

## Book Chapter

# The AIDSS Module for Aerial, Laboratory and Terrestrial Data Acquisition

Andrija Krtalić<sup>1\*</sup>, Milan Bajić<sup>2</sup>, Tamara Ivelja<sup>3</sup>, Ivan Racetin<sup>4</sup>,  
Vanja Miljković<sup>1</sup> and Dubravko Gajski<sup>1</sup>

<sup>1</sup>Faculty of Geodesy, University of Zagreb, Croatia

<sup>2</sup>PhD, Scientific Council, HCR – Centre for testing, development and training, Croatia

<sup>3</sup>Zagreb University of Applied Sciences, Croatia

<sup>4</sup>Faculty of Civil Engineering, Architecture and Geodesy, University of Split, Croatia

**\*Corresponding Author:** Andrija Krtalić, Faculty of Geodesy, University of Zagreb, 10000 Zagreb, Croatia

Published **April 15, 2020**

This Book Chapter is a republication of articles published by Andrija Krtalić, et al. at Sensors in October 2019 and February 2020. (Krtalić, A.; Miljković, V.; Gajski, D.; Racetin, I. Spatial Distortion Assessments of a Low-Cost Laboratory and Field Hyperspectral Imaging System. Sensors 2019, 19, 4267.) (Krtalić, A.; Bajić, M.; Ivelja, T.; Racetin, I. The AIDSS Module for Data Acquisition in Crisis Situations and Environmental Protection. Sensors 2020, 20, 1267.)

**How to cite this book chapter:** Andrija Krtalić, Milan Bajić, Tamara Ivelja, Ivan Racetin, Vanja Miljković, Dubravko Gajski. The AIDSS Module for Aerial, Laboratory and Terrestrial Data Acquisition. In: Xin-Wei Yao, editor. Prime Archives in Sensors. Hyderabad, India: Vide Leaf. 2020.

© The Author(s) 2020. This article is distributed under the terms of the Creative Commons Attribution 4.0 International License(<http://creativecommons.org/licenses/by/4.0/>), which

permits unrestricted use, distribution, and reproduction in any medium, provided the original work is properly cited.

**Acknowledgments:** This work was supported by the European Community's Fifth Framework Programme under the Information Society Technology Programme (FP5-IST): Project ID [2000–25044] - *Space and airborne mined area reduction tools* (SMART) and Project ID [2000–25300] - *Airborne Minefield Area Reduction* (ARC); the European Community's Seventh Framework Programme (FP7-SECURITY – Specific Programme 'Cooperation: Security'), under grant agreement No. [284747] - *Toolbox implementation for removal of antipersonnel mines, submunitions and UXO* (TIRAMISU); the Ministry of Science and Education of the Republic of Croatia under the programme Technology Projects (TP): Project ID [TP-06/0007-01] *Multi-sensor Airborne Reconnaissance and Surveillance in Crisis Situations and Environmental Protection*; the Office of Weapons Removal and Abatement in the U.S. Department through International Trust Fund for Demining and Mine Victims Assistance, Ig, Slovenia for projects *Deployment of the Decision Support System for Mine Suspected Area Reduction project* and *Deployment of the Decision Support System for Mine Suspected Area Reduction in Bosnia and Herzegovina*; *Mine action after the floods - regional synergy in emergency response, technology development and capacity building*, regional project of mine action centers of Bosnia and Herzegovina, Croatia, and Serbia, supported by Croatian Ministry for Foreign and European Affairs. HCR Centre for Testing, Development and Training Ltd. July 2014. The authors are especially grateful to the following people (listed in alphabetical order) who also participated in the module development and implementation: Tomislav Ban, Krešimir Božičković, Anna Brook, Tomislav Ciceli, Zlatko Čandjar, Željko Furjan, Dubravko Gajski, Hrvoje Gold, Čedomil Gros, Tihomir Kičimbači, Marko Krajnović, Davol Laura, Čedo Matić, Josipa Bogunović, Nikola Pavković, Željko Pračić, Ivan Racetin, Goran Skelac, Silvio Šemanjski, Ivan Šteker, Tajmin Tadić, Tomislav Vondraček, Željko Tkalčević, Mile Tomić, Roman Turšič, Dejan Vuletić, Sabine Vanhuyse, Yann Yvinec, pilots and technicians of the Croatian

Air Force, the Bosnia and Herzegovina Air Force and the RPAS and blimp pilots who participated in these projects.

## Abstract

The TIRAMISU Advanced Intelligence Decision Support System is an operational system proposed to Mine Action Centres worldwide for conducting non-technical surveys in humanitarian demining. The system consists of three modules, one of which is the module for data acquisition introduced and described in this study. The module has been designed, produced, improved, used and operationally tested and validated on several platforms (helicopters, RPAS and a blimp), with various sensors and acquisition units (GPS and IMU) in a variety of combinations for additional data acquisition from deep inside a Suspected Hazardous Area (SHA). For the purposes of aerial data acquisition over a SHA, the use of multiple sensors such as visible digital cameras and multispectral, hyperspectral and thermal infrared sensors are of benefit, because they display the scene in different ways. Off-the-shelf equipment and software were mostly used, but some specific equipment was developed (sensor pods, computerized imagery and data acquisition for sensors on board helicopters, computerized acquisition for sensors on RPAS, and on the blimp) and some software solutions (computer-controlled image sequence collection, IMU data acquisition, GPS data acquisition and real-time moving map visualization for navigation and acquisition, for transforming hyperspectral line scanner data into hyperspectral mosaics, and for producing hyperspectral cubes). The technical stability and robustness of the module were confirmed by operationally testing and evaluating the systems on the above-mentioned platforms and missions in several actual SHAs in Croatia and Bosnia and Herzegovina, between 2001 and 2015. The adaptation of an existing aerial hyperspectral imaging system in a low-cost setup for collecting hyperspectral data in laboratory and terrestrial field environment was also conducted. The imaging spectrometer system consists of an ImSpector V9 hyperspectral pushbroom scanner, PixelFly high performance digital CCD camera, and a subsystem for navigation, position determination and orientation of the system in space, a sensor

bracket and control system. Image acquisitions indicates that this hyperspectral system has potential in archaeological and agronomic applications.

## Keywords

Multi-Sensors System; Aerial Data Acquisition; Sensors; Platforms; Remote Sensing; Imaging Spectrometer; Hyperspectral Imaging

## Introduction

After the end of the Homeland War in 1995, the Republic of Croatia faced a huge mine problem. A great deal of its territory (about 10.5% [1]) was considered to be suspected hazardous areas (SHAs). “A Suspected Hazardous Area (SHA) is an area where there is reasonable suspicion of mine/Explosive Remnants of War (ERW) contamination on the basis of indirect evidence of the presence of mines/ERW” [2]. During the post-war period, concern increased regarding the number of landmine injuries happening to innocent civilians. The civilian approach to demining (humanitarian mine action) differs from the military approach and begins when the conflict stops. It is called mine action [2]. The goal of integrated mine action is to return previously mined land to the community for use, and covers a far wider scope of activities than simply mine clearance. It includes mine awareness and risk reduction education, minefield surveying, mapping, marking and clearance, victim assistance, including rehabilitation and reintegration, and advocacy to stigmatise the use of landmines and support a total ban on anti-personnel landmines [3]. Mine action ultimately aims at a 100% clearance rate of land mines and dangerous explosive objects [3]. To plan and implement demining projects successfully, it is necessary to know minefield locations. Information-gathering techniques, such as interviewing returnees, general mine action assessment [4], technical surveys [5], analytical evaluation of military maps or reading the biographies of military commanders, provide a good insight into the mine situation, [6,7]. However, as noted in [3] these are long, expensive processes that ultimately do not provide enough accurate

information. The mine action process must be accelerated in order to identify mined areas quickly, avoid accidents, and assign demining priorities. This requires a quick, low-risk, cost-effective tool for surveying SHAs and producing maps with indicators of mine presence (IMP) and absence (IMA) [8-10] to define SHA boundaries. For example, in the Republic of Croatia, humanitarian mine campaigns have shown that only 10% of SHAs are actually mine-affected [11]. It is almost as important to identify areas not affected by landmines, for the purpose of reducing an already defined SHA [12].

To this end, the Advanced Intelligence Decision Support System (AIDSS) [13,14] based on low-cost solid-state digital cameras, and thermal and hyperspectral sensors, has been designed, produced, operationally validated and implemented in the Republic of Croatia and Bosnia and Herzegovina. AIDSS is the result of research conducted within 7 international and domestic scientific projects: ARC [15], SMART [12], System for Multi-sensor Airborne Reconnaissance and Surveillance in Crisis Situations and Environmental Protection [16], Deployment of the Decision Support System for Mine Suspected Area Reduction [17], Deployment of the Advanced Intelligence Decision Support System for Mine Suspected Area Reduction in Bosnia and Herzegovina [18], TIRAMISU [19], which aimed to implement airborne and satellite-borne remote sensing for non-technical survey [10,20] in humanitarian mine campaigns and crisis situations. AIDSS is a modular tool with a module for aerial data acquisition [14], and Impact of Flooding on Mine Action in Bosnia and Herzegovina, Croatia, and Serbia, funded by Republic of Croatia [21].

The goal of the AIDSS Module for aerial data acquisition, or any similar multi-sensor imaging system, is to provide usable images for extracting information, detecting and identifying objects and features based on image (geometric and spectral) characteristics, and classification as shown in [12,13]. Multi-sensor imaging systems as cited in [22-26] allow the implementation of multi-sensordata fusion [27,28], the results of which can reveal certain objects indirectly, as shown in [29]. Multi-sensor fusion deals with a combination of complementary, sometimes competing

sensor data, in a reliable estimate of the environment, to achieve an outcome which is better than the sum of its parts, [30-32], to achieve inferences that are not feasible from each sensor operating separately. Advances in the development of sensor technology are insufficient without the use of multi-sensor fusion techniques [33]. Since sensors of different types integrated in the system have their own limitations and perceptive uncertainties, an appropriate data fusion approach is expected to reduce overall sensor uncertainties and increase the accuracy of system performance [34]. The crucial thematic framework which assures operational success and the outcome values of multisensory imaging and fusion for the purposes of anti-mine operations is the detailed identification of the mined scene, with the working title of analytical assessment, defining the so-called strong indicators of mine levels, introduced in 2001 and developed up to 2015 [6,7]. These paradigms have assured the selection and adaptation of sensory techniques, a regime for recording situations in SHAs, and a new type of outcome, called 'office virtual reconstruction of former battlefields'.

Data fusion in AIDSS is not performed within the data acquisition module, but after processing the collected materials in the third module [14]. Here, it is important to stress that data fusion is not performed in real time, as with other multi-sensory systems, for example [21,35]. Therefore, it is important to define the purpose of multi-sensory imaging well, in order to select optimal sensors and adequate platforms for such a system.

A thorough review of satellite and airborne sensors for remote-sensing-based detection of minefields and landmines can be found in [11], focusing on multi-temporal aerial photographs and satellite images. The paper presents a good analysis of the structure and composition of minefields and patterns that can be obtained for minefield detection. On the other hand, [33,36,37] focus on some of the most common 'direct' remote sensing technologies in landmine detection, defining 'direct' as mine clearance per se (a technology used in technical surveys and actual demining processes). The demand for detailed information from inside SHAs has increased markedly throughout the world. Therefore, it is very important to develop new remote sensing

techniques that allow for the direct measurement of common situations in SHAs. Although public satellite imagery is available (e.g. Sentinel, Landsat), low ground sample distance - GSD (10 m for Sentinel-2 and 30 m for Landsat satellite imagery) is an obstacle to interpreting and extracting information with the required accuracy. On the other hand, commercial satellites provide better GSD ( $\approx 0.5$  m from WorldView and GeoEye satellite imagery) and better insights into the scene. Airborne imagery resolves the low GSD problem of satellite imagery and, with better GSD, provides adequate spectral bands for photogrammetric and remote sensing methods. RPAS provide special advantages over other platforms, in particular high GSD, and more economical preparations for performing and collecting data in smaller areas. Examples of RPAS use in landmine detection can be found in [38-40], and IMP detection in [41,42].

This chapter presents an overview of the development of an imaging system operating in the visible, near infrared and LWIR range of the electrical spectrum according to defined needs, particularly humanitarian mine action, and which has also been tested to collect data on the quality of standing water, oil pollution in the Adriatic and fire monitoring [16,43]. The results of this system are used as inputs in data fusion and the production of mine danger maps [6,7,10,14].

This chapter also describes the design of a low-cost hyperspectral system for laboratory and field (terrestrial) data acquisition, which collects sequential continuous samples to create a 3D image (hyperspectral cube). It is one result of research conducted within four international and domestic scientific projects: Airborne Minefield Area Reduction (ARC) [44] Space and airborne mined area reduction tools (SMART) [12], System for Multi-sensor Airborne Reconnaissance and Surveillance in Crisis Situations and Environmental Protection [16] and Toolbox implementation for removal of antipersonnel mines, submunitions and UXO (TIRAMISU) [18] within the domain of humanitarian mine action and crisis situations. Its primary application was airborne collection of hyperspectral information [45], then creating a 3D image from continuous

samples [46] of suspected hazardous areas, and examining the possibilities of distinguishing vegetation growing over buried mines from vegetation growing outside minefields using spectral reflectance data [47]. Since we are dealing with gathering hyperspectral data on small objects at close distances (up to 3 m), the geometric reconstruction needs to be accurate in order to detect small differences in the spectrum for objects of interest. Hence, calibration of the developed linear hyperspectral system was carried out. Calibration of linear sensors is usually done by simulating an array sensor [48] and we used the method described and presented in [49,50] was applied in this work. The modulation transfer function (MTF) [51] is the most frequently used scientific method for describing the performance of optical systems. There are many solutions for calculating MTF, but they are based on determining the parameters for 2D images [52-54]. Due to the specifics of the linear scanner and aim of determining imaging quality at certain wavelengths, spatio-spectral MTF was performed in this work.

Finally, the examples of hyperspectral imaging of archeological artefacts in the laboratory environment and imaging of vineyards in the field environment with the system are presented. These data are then forwarded to various kinds of experts and could provide them with useful insights and new information.

## **AIDSS Module for Aerial Data Acquisition**

AIDSS is not a mine detector. It is a set of tools and methods, advanced and integrated into one effective system, and based on SMART methodology [55] for use by experienced operators, experts in remote sensing and experts from Mine Action Centres, to help SHA reduction using remote sensing data and expert knowledge [14]. In the SMART project [56], many useful tools for aerial non-technical surveys in humanitarian mine action were developed and tested, but within the actual project and following it, they were integrated and implemented operationally. Due to actual demands for help in removing mines quickly in the Republic of Croatia, and the desire to continue using the tools, a project was prepared and implemented [57] with AIDSS as the result. AIDSS is a complex system (Figure 1)

to support decisions on defining SHAs. It consists of three modules:

- Module for the analytical assessment of mine information system (MIS) data,
- Module for data acquisition (multi-sensor imaging system),
- Module for data pre-processing and processing.

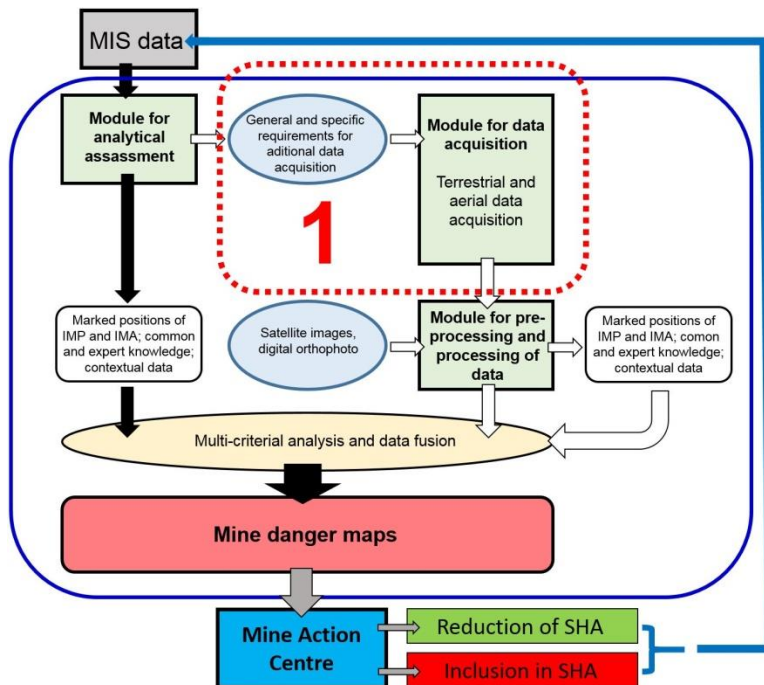


**Figure 1:** Scheme of AIDSS methodology. 1 – Module and requirements for data acquisition.

The modules can be used together or individually. Input includes data from the Mine Information System (MIS), expert knowledge, and airborne, satellite and contextual data (Figure 1). AIDSS is a unique mine action technology that provides a successfully operational system combining remote sensing with advanced intelligence methodology. It is a validated operational solution for non-technical surveys in humanitarian mine actions [13] proposed to Mine Action Centres worldwide, because it is

adaptable to specific terrains and situations. The outcomes of this system are successfully detected and confirmed geographical positions of IMPs and IMAs, better (re)definition of SHA, and thematic maps (mine danger maps) [6]. So, the AIDSS module for data acquisition is a very important part of the whole system.

The goal of the AIDSS module for data acquisition for humanitarian mine action is to collect information about the current situation within a SHA or munitions depot destroyed by explosion, that is, information on the locations of remains of fortification objects in the area. Fortification objects are strong IMPs, such as trenches, bunkers, artillery tool stores, personnel shelters, altered forest boundaries, objects that are not currently used but were used before the conflict, and the remains of military equipment. The data collected in the module show the actual situation in the SHA and can be used to confirm existing data stored in MIS. So they are collected on the basis of general and specific requests for data acquisition, which are the result of the analytical assessment of existing data on the SHA carried out by experts in mining and combat in a certain geographic area, along with the staff of MACs [7]. A general request for data acquisition in a SHA requires detecting IMPs on images for a particular geographic area. On the other hand, specific requests refer to locating IMPs for which certain information is already available (through interviewing returnees and participants in conflicts), but for whatever reason, it has been impossible to get close and confirm their presence on the ground. SHAs in the Republic of Croatia are usually not compact areas with regular borders, but larger and smaller fragmented areas (Figure 3, Nos. 3, 5 and 7). For this reason, helicopters and remotely piloted aircraft systems (RPAS) were chosen as platforms, and a blimp was also tested as potential platforms. Helicopters are mobile platforms which can change direction and require low minimum speeds for stable flight (Mi-8  $\approx$  120 km/h, Bell-206  $\approx$  70 km/h) in comparison with airplanes. Helicopter flights require shorter times, particularly in manoeuvring from one site and set of images to another. Helicopters can also fly lower ( $\approx$  200 m above the ground for minimum speed flight stability, and this directly affects the size of GSD on images. For an even better view of details in small areas of SHAs, or in parts recorded from

helicopters where GSD was inadequate to detect individual IMPs, RPAS was used as a multi-sensor system platform. These platforms can fly low and hover over areas of interest within a SHA.

Research and development to create AIDSS has responded to real demands from humanitarian mine action experts in Croatia. It was done using prototyping (spiral) methodology rather than waterfall, and the statement of needs was defined before each step was defined, followed by state of the art, and ending with gap-filling requirements. Radar technology was not considered within the scope of AIDSS research. But we encountered aerial radar technology in the SMART [58], and TIRAMISU [59,60] projects. Synthetic aperture radar from SMART was used in 2001. It had four wavelengths, polarization modes, and showed the potential to distinguish between several kinds of target (trenches, pioneering vegetation invading former cultivated areas). Between 2001 and 2019, significant advancement in radar technology occurred which could be applied to mine action, even for the direct detection of land mines, e.g. [61]. However, the most important aspect was that AIDSS could use in a non-technical survey, not for locating mines, but strong IMPs, and it could be used in synergy with other technologies applied in humanitarian mine action.

The development and use of this aerial multi-sensorsystem for data acquisition started in 2001 as part of the ARC project. This first system was installed on a Bell-206 helicopter (Figure 2). AIDSS and a module for aerial data acquisition was conceived, developed, installed, tested and used on a Mi-8 helicopter between 2008 and 2012 (Figure 5). Further development, testing and use were implemented within the TIRAMISU FP7 project [18,62] and mine action after flooding, a regional response to the crisis, and a technology development and capacity-building project funded by the government of the Republic of Croatia. The module ensured the stability and reliability of data acquisition on each platform. The technical stability and robustness of the system were confirmed by testing and evaluation (based on the behaviour of the system during data acquisition over areas of interest) on different platforms and

missions in the Republic of Croatia and Bosnia and Herzegovina in the periods mentioned.

The AIDSS module for data acquisition consists of:

- Visible digital cameras
- A multispectral camera
- An LWIR camera
- A hyperspectral sensor
- Navigation devices (iMAR, GPSs)
- Industrial computers, laptops (for navigation and iMAR management)
- Monitors
- A power supply system (batteries or system to retrieve the current from the platform).

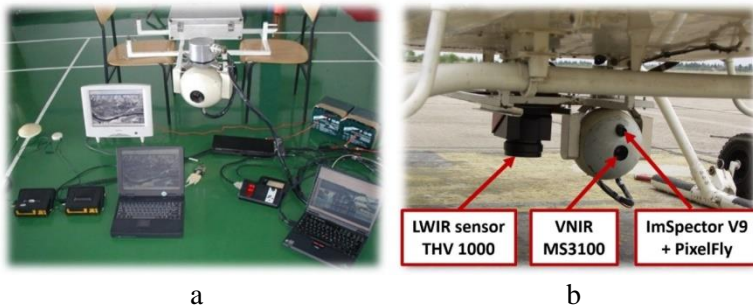


**Figure 2:** The first multi-sensor system for aerial data acquisition: a) navigation, control and power supply components, b) sensors: THV 1000, MS3100 and ImSpector V9 + PixelFly installed on a Bell-206 helicopter.

## Sites where AIDSS was Implemented

Between 2001 and 2015, in the Republic of Croatia, various airborne systems were used to gather data on SHAs, among other things, in the following locations: Glinska Poljana (Milekovići), Pristeg (Vrankovići), Bilje, Drniš, Gospić and Murgići; a destroyed munitions depot in Pađene; the quality of standing water in Lake Jarun in Zagreb; a mine testing site near Benkovac, and oil pollution in the Adriatic. The data and its usefulness will be presented in what follows in order to describe

the potential of the AIDSS module for airborne data acquisition and implementation.

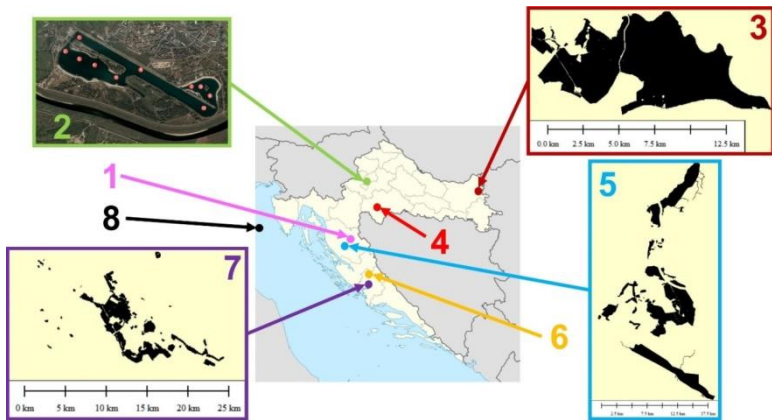


**Figure 3:** Areas where multi-sensorsystems for data acquisition were applied: 1) part of the SHA near the village of Murgiči, 2) Lake Jarun in Zagreb, showing locations where the coefficient of reflectance in situ were measured sporadically from a flotation device on the lake (red dots), 3) an SHA in Bilje municipality (black polygon), 4), part of an SHA near the village of Glinska Poljana, 5) an SHA in Gospić municipality (black polygon), 6) the area of the destroyed munitions depot in the village of Pađene, 7) an SHA in Drniš municipality (black polygon), 8) oil pollution in the Adriatic.

Trial continuous airborne data acquisition for the purpose of testing the use of multi-sensor systems for non-technical surveys in humanitarian mine action was carried out on 16 and 23 April 2003 as part of the ARC project [63]. Data acquisition was carried out in the area and surroundings of Glinska Poljana (Milekovići) and Pristeg (Vrankovići). Glinska Poljana is in central Croatia (Figure 3, No 4), in a highland area with gentle hills and a continental climate. Pristeg is in southern Croatia, twenty kilometres southwest of Pađene (Figure 3, No 6), in a highland karst area. According to MIS data, the number of known mine records and their contents indicates both areas are highly contaminated by mines.

Lake Jarun in is the city of Zagreb (Figure 3, No 2). The need was expressed to test and monitor its water quality using hyperspectral airborne image processing. Data acquisition in the area was carried out as part of a project [57] in 2008. In the

autumn of that year (12-19 October) data was gathered to confirm the existence of oil pollution in the Adriatic within the Ecological and Fisheries Protection Zone (Figure 3, No 8) in two regimes: a) based on notifications from the CleanSeaNet European Maritime Safety Agency, and b) for search purposes.

Within the project, [64] data were gathered on SHAs in the municipalities of Bilje, Drniš and Gospić. The data acquisition took place from 26 March to 10 April. Bilje (Figure 3, No 3) is in the far east of the Republic of Croatia, in the Pannonian plain. It is an exclusively flat area with a large percentage of marshland. Data were gathered on 36.1 square kilometres (sq km) of SHA in the municipality, most of it marshland bordering with the Republic of Serbia. Drniš is in the south of the Republic of Croatia in a hilly, karst region. Data were gathered on 12 sq km of SHA in the municipality. Gospić (Figure 3, No 5), with the hamlet of Murgići (Figure 3, No 1), is located in Lika-Senj County in central Croatia. Data were gathered on 56.8 sq km of SHA in the municipality, representing 5.9% of its total surface area.

The munitions depot in Padjene (near Knin) exploded on 13 September 2011 due to an intense forest fire. The depot itself was totally destroyed and unexploded ordnance (UXO) was scattered around it. The village of Padjene is in the south of Croatia (Figure 3, No 6) in hilly, karst terrain overrun with low vegetation (maquis). Data were gathered as part of the project [62] on two occasions. The first was in 2002 and was in order to gain a better insight into conditions in the terrain. The second was in 2015 with the aim of gaining a better insight into conditions in the terrain after clearance.

## Platforms

Mi-8, Bell-206 and Gazela helicopters, UAV X8 MK and UAV 8 ZERO and a blimp (Figure 4) were operationally tested over the sites in question.



**Figure 4:** Platforms for aerial data acquisition system of AIDSS and sensor pods (in the green ellipses) on a) Mi-8 helicopter, b) UAV 8 ZERO, c) Bell-206helicopter, d) UAV X8 MK, e) blimp, and f) Gazela helicopter.

## Helicopters

The first platform used in 2003 for an aerial multisensory system during the trial data acquisition on the current situation in the SHAs (Glinska Poljana and Pristeg), as part of project ARC, was a Bell-206 helicopter. The crew comprised the pilot, co-pilot and two systems operators. Based on the results and experience gained, the first AIDSS module for aerial images acquisition was planned, made and used on a Mi-8 military helicopter (Figure 4 a) and a Bell-206 (Figure 4 c). The crew of the Mi-8 comprised the pilot, co-pilot, technician, systems operator, navigator and mission leader (it is possible to increase the number of people involved in each segment of the system). In order to extend the system and increase the amount of equipment carried, the current crew consists of three members, the pilot, co-pilot and systems operator. The maximum endurance (along with an additional tank of fuel inside the helicopter) of the Mi-8 is 4 hours 15 minutes, and of the Bell-206, 2 hours 15 minutes. So, if the

endurance is at least 3 hours for the Mi-8 (1 hour 15 minutes for the Bell-206) it is theoretically possible to acquire high-resolution multi-sensor imagery from an area of about 45 sq km ( $\approx 25$  sq km for the Bell-206) per flight over flat terrain, at a relative height of 1000 m in one continuous sequence, without loops. The Gazelle helicopter (Figure 4 f) was used in Bosnia and Herzegovina in 2014, and is capable of transporting up to five passengers, with 500 kg of internal space in the rear of the cabin. There was a particular advantage when using the module, as the helicopter already had an opening in the floor, which made it easier to install the equipment without compromising the flying ability of the platform. In operational conditions for data acquisition over an area of 105 sq km (in an area of 900 sq km) of SHAs in Bilje, Drniš and Gospić, 16 hours and 30 minutes of effective flying time were required (not including the flight to the location and return to the airport). Planning the flight route was complicated by the fact that the SHAs are not one compact area, but fragmented over a large area (Figure 3, No 3, 5, 7), so the acquired data covered a much larger area than the area of interest (105 sq km). Parallel flight routes were planned and performed at different altitudes, repeated over certain areas. The standard flight altitude selected was 600 m above the mean terrain altitude, as these parameters proved the best and most economic for planning the flight route and the time required to take the images in each pass (Figure 12). At that altitude, GSD for the visible digital cameras was  $\approx 7$  cm, multispectral sensors  $\approx 17$  cm, for the LWIR sensor  $\approx 45$  cm, and for ImSpector V9  $\approx 16$  cm (Figure 12 a). As part of the effective flight time spent in the air, supplementary flights were carried out to get better GSD (lower altitude flights), that is, a better insight into the terrain, where necessary.

### **RPAS and Blimp**

Since the SHAs were not compact, but comprised a large number of scattered areas, as already mentioned, (Figure 3, No 3, 5, 7), and in the interests of economising resources for data acquisition on such areas, several RPAS platforms were tested for the specific task of collecting high spatial resolution hyperspectral data. For this purpose, the TIRAMISU Light Hyper Spectral

Imaging System (T-LHSIS) for aerial data acquisition was developed, installed and tested on two RPAS platforms, UAV X8 MK and UAV 8 ZERO, and a blimp [47]. Both multirotor UAVs tested fall into the category of small UAVs with take-off mass below 10 kg. UAV X8 MK was tested on several occasions at several locations. The main problem in this project [62] was to provide RPAS for a payload of about 4 kg with several additional requirements related to collecting hyperspectral data with a line scanner. Today, the problem no longer exists. The requirements for any platform used for hyperspectral survey for the purposes of vegetation stress inside and outside mine-contaminated areas are:

- Flight velocity - as low as possible
- Flight altitudes - as low as possible (depending on the size of the observed object)
- Swing and vibration - minimal for obtaining correct geometric images
- Controllability of platforms and navigation during flight, or GPS tracking during flight (flying the given routes and controlling the coverage area with images).

## Sensors

Various types of sensors (multispectral: Fuji FinePix, Canon 5D, Nikon D90, SONY  $\alpha$ 6000, DuncanTech MS3100, Redlake MS4100; hyperspectral: ImSpector V9/PixelFly, UHD; LWIR: THV 1000, Photon 320) were investigated. A wealth of experience was gained, and random selection was narrowed down while refuting the frequently expressed claim, “the more data from different sensors, the greater the probability of success” [37], (CROMAC-CTDT, 2008). No single technology has the capability to detect and recognise a variety of IMPs under all circumstances [33]. Most developed technologies and techniques are complex and/or expensive. Many are promising, but none has the sensitivity, size, weight, manufacturability and price range required for humanitarian mine action [33,37]. The goal of the AIDSS module for data acquisition is to collect information about the current situation within a SHA or munitions depot destroyed by explosion, that is, information on

the locations of remains of fortification objects in that area. Fortification objects are IMPs, such as trenches, bunkers, artillery tool shelters, personnel shelters, altered forest boundaries, objects that are not currently used but were used before the conflict, and the remains of military equipment. Sensors for the AIDSS module for data acquisition were selected according to the above requirements. IMPs can be detected and isolated on digital images using some of the methods for processing digital images described in [65,66], or by methods of object-oriented identification of linear objects based on presuppositions regarding their geometric and radiometric features and use of various filters to emphasise them [67-69]. Isolating IMPs on hyperspectral images is done via their spectral characteristics, as shown in [47,70,71].

**Table 1:** Technical specifications of the visible cameras: Nikon D90 [72], Sony  $\alpha$ 6000 [73], and multispectral cameras: DuncanTech MS3100 [74], Redlake MS4100 [75].

Camera	Sensor type	Sensor size (mm)	Number of Pixels / Effective Pixels	Pixel size ( $\mu\text{m}$ )	Max image size (pixel)	Radiometric resolution (bit)	Frames per second
Nikon D90 DX	CMOS	23.6 * 16.8	12.9/12.3	5.5	4288 * 2848	12	4.5
Sony $\alpha$ 6000	APS-C	23.5 * 15.6	24.7/24.3	3.9	6000 * 4000	12	11
DuncanTech MS3100	3 * CCD	7.6 * 6.2	1.4	4.65	1392 * 1039	8 and 10	7.5
Redlake MS410	3 * CCD	14.2 * 8	2	7.4	1920 * 1080	12	10

## **Visible Digital Cameras**

Visible digital matrix cameras in the present constellation of sensors are the Nikon D90 and SONY  $\alpha$ 6000, which collect information in the visible part of the spectrum, in 3 spectral bands from 400 - 700 nm. The cameras' technical specifications are listed in Table 1. The Nikon D90 has high signal-to-noise components and design, and delivers exceptional performance, even at high ISO setting and GPS unit to provide automatic real-time geo-tagging [72]. It was included in the sensor system for the AIDSS data acquisition module due to its robustness and technical characteristics. The Sony  $\alpha$ 6000 E-mount camera is a compact, light-weight camera with interchangeable lenses. The  $\alpha$ 6000 compares favourably to bulkier, heavier DSLRs, and with interchangeable lenses, manual controls and more, users sacrifice nothing [73]. This is very important when selecting sensors for an aerial multi-sensor imaging system, as the payload can be reduced, which is important when constructing supports for an unmanned aerial vehicle (UAV) and calculating endurance without reducing the quality of the images collected. These parameters and the camera's ability to freeze a subject at an amazing 11 fps [73] for shots that capture the exact moment or object of interest, were decisive factors in its selection.

## **Multispectral Sensors**

The DuncanTech MS 3100 (Table 1) was the first multispectral sensor to be used for trial data acquisition with the aim of using a multi-sensor system for non-technical surveys in humanitarian mine action in 2003. The camera has a colour-separating prism and three imaging channels that allow simultaneous image acquisition in 3 - 5 spectral bands through a common aperture. Image sensors are CCD array sensors with spectral sensitivity ranging from 400-1000 nm. The resulting images are co-registered, providing excellent image quality and colour fidelity [74]. In 2009, a next-generation sensor was introduced into the module. The Redlake MS-4100 (Table 1) is a multispectral optical matrix camera with 3 separate CCD sensors and is available in two spectral configurations. The first is RGB for high quality colour imaging, and the second is colour-infrared

for multispectral applications (3 spectral bands from 400 - 1000 nm). Standard colour-infrared imaging (CIR) uses red, green and near-infrared bands approximating Landsat satellite bands. The maximum frame of the MS-4100 is 10 fps with a pixel clock rate of 25 MHz and bit depth of 12 bits [75].

## **Hyperspectral Sensors**

Conventional commercial spectrometers or spectrophotometers are usually able to measure the optical spectrum from a specified surface area as one point [76,77]. This is done either with one detector scanning the spectrum in narrow wavelength bands, or with an array detector, in which case all the spectral components are acquired at once. If the spectrum is to be measured at several spatial locations of the specified surface, the target under examination or the measuring instrument must be mechanically scanned. In the next section, the procedure will be shown for creating a hyperspectral sensor which creates an image from sequential, continuous samples (hyperspectral cube).

An imaging spectrometer instrument, based on an imaging spectrograph like the ImSpector V9, is 'an instrument capable of simultaneously measuring the optical spectrum components and the spatial location of an object surface' (Spectral Imaging LTD, 2003). The ImSpector V9 hyperspectral line scanner is a direct sight imaging spectrograph and was combined with a PCO PixelFly high performance digital 12bit CCD monochrome matrix camera [78] to form a geometric sensor model – imaging spectrograph constructed for this particular module. The PixelFly matrix camera with a scan area of 8.6 \* 6.9 mm and effective pixels of 1280 (H) \* 1080 (V) consists of an ultra-compact camera head, which either connects to a standard PCI or a compact PCI board via a high-speed serial data link. The available exposure times range from 5  $\mu$ s to 65 s [78].

Another hyperspectral sensor was used in the trial, the Cubert UHD 185 - Firefly (Cubert). This hyperspectral full-frame camera simultaneously records 125 bands between 450 and 950 nm with 50 by 50 hyperspectral pixels in one frame acquisition and 8 nm spectral resolution. At the same time, a panchromatic channel of 1000 \* 1000 pixels is recorded. With the software

provided by the manufacturer, the hyperspectral pixels may be pan-sharpened to the greyscale image's resolution. The hyperspectral cube rate is up to 5 cubes/s. The hyperspectral cube parameters (image and pixel size), depending on the lens used, are shown in Table 2.

**Table 2:** Parameters of UHD -185 camera and corresponding hyperspectral cubes for suggested altitudes.

Lens	Distance (m)	Image diameter (m)	Theoretical GSD (m)	Diameter of the spectral pixel (m)
Focal length = 10 mm Aperture = 33°	50	32.97	0.033	46.62
	100	65.93	0.066	93.24
	300	197.8	0.198	279.73
	500	329.67	0.330	466.22

### Thermal Infrared Sensors

The first LWIR sensor used in the development of a multi-sensorsystem (between 2001 and 2008) was the Thermovision 1000 FLIR (THV 1000). It is a compact high definition real time thermal imager operating in the 8 – 12  $\mu\text{m}$  region of the electromagnetic spectrum. The record is made by serially scanning the scene, vertically using a vibrating mirror, and horizontally, using a multi-angled mirror. During one horizontal scanning of the scene, it collects data in five parallel linear elements of the detector. The length of the detectors is 700  $\mu\text{m}$ . The system creates and stores 25, 8-bit digital images (600 \* 400 pixels) per second. A frame grabber is required to create the digital images. The lens fields of view are 5°x3°3 and 20°x13°33, and the temperature range is from -15° to +55°C. A FLIR Photon 320 (FLIR Systems, Inc. the USA, [www.flir.com](http://www.flir.com)) LWIR (8 – 14  $\mu\text{m}$ ) uncooled microbolometer camera was used for collecting thermal images from 2008 until now. The Photon 320 had a 50 mm lens providing a 14° horizontal and 11° vertical field of view and acquired image frames of 324 × 256 pixels as raw 14-bit digital numbers at the rate of 9 Hz. Image sequences from the camera were converted into ethernet data packets by the FLIR Ethernet module and this data was then stored on a computer on the platform. The system time of the

computer was set to GPS time prior to flight, so that the thermal data files could be synchronized with GPS log files.

### **Sensors for Navigation and Positioning**

The system for navigation, determining the position and orientation of the system in space, consists of a single-frequency GPS device integrated with an inertial measurement unit (IMU) iVRU-RSSC by iMAR GmbH, and additional GPS units arranged in or on the platform. iVRU-RSSC is a triple-axis inertial system with three mutually perpendicular MIL-MEMS gyroscopes for determining the angle elements of the spatial orientation of the sensor, and 3 MEMS-accelerometers to determine the acceleration components along all three axes. The device has an integrated microprocessor for 16-bit digitalization of data from the sensor and deviation correction, to improve the accuracy of all measured elements. The GPS device is used in an absolutely cinematic mode with WAAS and EGNOS differential corrections. The GPS data are used primarily to correct navigation solutions acquired from the inertial system. Although the internal IMU working rate is 200 Hz, for this purpose, the elements of current position and sensor orientation in relation to the referential WGS84 coordinate system were stored with a frequency of 20 Hz. This allowed high quality fluctuation and raw element bias correction using the internal processor. On the other hand, the volume of redundant data was reduced, and further processing was made easier, since the frequency of imaging of the ImSpector V9 sensor is 10 Hz. The elements of the external orientation of the platform related to the WGS84 coordinate system, expressed in ellipsoidal coordinates  $\varphi$ ,  $\lambda$  and  $h$  on the GRS80 ellipsoid. Alongside the IMU, a special GPS device was used with an aerial to synchronize the computer time with the GPS time (UTC) (Figure 7).

### **Module Control System**

The image capture rate was controlled by an operator inside the helicopter or remotely from the RPAS flight control board. A special command desk was made to gather data from the Mi-8 helicopter (Figure 5) to manipulate the module. Up to 2009,

desk-top computers were used to manage sensors in helicopter platforms. Due to vibration (particularly in the Mi-8) the computers crashed from time to time and communication with the sensors was lost. So, the desktop computer has been replaced by industrial controllers with solid state drives (SSD) which are more robust and resistant to vibration. Small, custom-made computers were used for the sensor control on RPAS platforms. The Nikon and Sony cameras were operated in shutter priority mode (a fast shutter speed was required to minimize motion blur), in which the desired shutter speed (depending on the altitude and speed of the platform and light) was set before flight and the exposure was adjusted automatically by varying the aperture. Images from the Sony  $\alpha 6000$  camera were captured in RAW format and stored on the memory card in the camera for post-flight download.

The ImSector V9 + Pixelfly hyperspectral system was managed using the RECORDER programme, which was developed and produced specially for the ARC project. It includes individual images exported to standard TIFF format, and the metadata for each image are stored in the corresponding table (time of recording, GPS and INU data). Based on these data, synchronization with GPS and IMU data is performed.



**Figure 5:** Control table with module control system component inside Mi-8 helicopter: 1) PC for manipulation with Nikon D90 and Photon 320; 2) Monitor for PC and industrial controller (switching is performed as needed during recording); 3) Laptop for manipulation with IMU, 4) Industrial controller for manipulation with MS4100 and ImSector + PixelFly (not part of the first system configuration, built in 2009); 5) Junction box of the electric power system, 6) Converter from 28-30 V DC to 220 V AC for PC and monitor; 7) Large battery (210 Ah, 75 kg) for power supply; 8) Cables for connection with sensor, 9) Navigation monitor located in the cockpit.

## Module Power Supply

The acquisition systems on board the Mi-8 and Bell-206 helicopters used their own sources of electric power, but on the Mi-8, could also use electricity from the helicopter's power supply system. Previous practice has shown certain problems when connecting to the helicopter's electrical system (a special type of connector is needed, equipment is subject to obsolescence, and installation is impossible on helicopters which are over 50 years old). It is therefore essential to ensure the independence of the system's power supply from the platform's power supply. The variety of electrical power sources used in the helicopter also decreases the operational availability of the system. A continuous, stable electricity supply for aerial data acquisition is mandatory. It is also essential for the stable, continuous operation of the module during flight. The major obstacle in this regard was the need to convert electricity from 28-30 V DC to 220 V AC 50 Hz (in the initial variant of the system). Therefore, the power supply for the module for aerial data acquisition was re-designed in 2012. This was done by replacing the desktop PC with two industrial controllers (one was already embedded in 2009) and a monitor operated by 24 V (controllers) and 12 V (monitor) DC. The instruments and equipment for the modules on the helicopters were powered by an independent power supply consisting of two large batteries (210 Ah, 75 kg each) in the Mi-8 helicopter and one in the Bell-206 helicopter. Small batteries were used to power a module installed on the RPASs.

## Production and Parametric Georeferencing of the Hyperspectral Cube

The robust structure of ImSpector V9 suits both industrial and scientific applications that require rapid, precise spectral measurements at low cost. The last configuration in AIDSS uses a narrow slit (8.8 mm x 50  $\mu$ m) at the front end of the optical system and enables a spectral resolution of 4.4 nm of 80 channels in a spectral range from 430 nm to 900 nm. At the nadir, the system provides mapping of a narrow strip  $(0.333 \cdot H) \cdot (0.0028 \cdot H)$ , where H denotes the height above

ground. The scanner was used to acquire reflectivity samples from the SHA in several different types of terrain. The usefulness of the radiance is limited, due to its strong dependence on illumination, which can change during the acquisition mission. Thus, we did not attempt to measure the radiance, but calculated the reflectance coefficient. The reflectance coefficient is the ratio of the volume of electromagnetic waves recorded by the sensor to the volume of electromagnetic waves recorded by an aerial near the sensor. It is a property of the observed material and is equivalent under different illumination conditions. The spatial accuracy of airborne discrete measurements depends on the platform movements, positioning accuracy, and orientation system. When the system is placed on a mobile platform, it is possible to scan the terrain linearly, from the interval of line  $\Delta s$ . The interval of line  $\Delta s$  depends on the flight speed and frequency of storing  $f_s$  images in the acquisition system (Figure 6 a). Using the hyperspectral sensor and parameters, recording is manipulated via Recorder software. For example, with a flight height of 750 m, vertical binning  $\times 1$  (for storage, the entire surface area of the PixelFly sensor is used),  $w = 218$  m, GSD = 0.19 m. With a flight speed of 120 km/h (33.3 m/s), the frequency of image storage is  $f_i = 20$ , and the interval between the lines is 1.6 m.

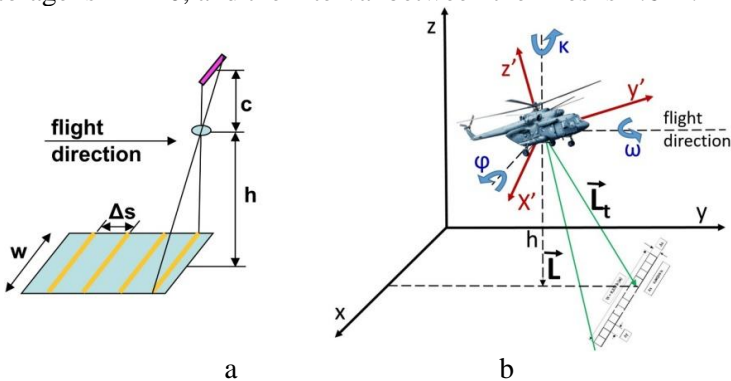


**Figure 6:** a) Geometry of transference of the ImSpector V9 and PixelFly hyperspectral systems, b) Transformation of theoretical view vector  $\vec{L}$  to effective view vector  $\vec{L}_t$ .  $\kappa$ ,  $\omega$  and  $\phi$  denote roll, pitch and true heading angles respectively.

To use the line scanner in full imaging mode (acquiring contiguous scan lines), it is necessary to find the optimum

ground speed of the platform. It is a function of the required GSD and scanner imaging frequency, according to a simple equation (1) used to arrive at optimum distance per second [46]:

$$GS = GSD/f_i \quad (1)$$

where are:

- GS = Ground Speed of the platform in [m/s],
- GSD = Ground Sampling Distance in [m] and
- $f_i$  = Imaging scan period in [s].

The maximum frame per second is around 24 Hz and depends on radiometric parameters during collection reflected radiation (exposure time and sensor sensitivity). Line scanning of the V9 hyperspectral sensor demands a very complex calibration procedure and time-consuming processing (Figure 6 a). Software solutions in the Matlab package have been developed to produce a raw hyperspectral cube, which is then parametrically decoded using the PARGE 2.3 software package [79]. The procedure for parametric geocoding means assigning precise spatial positions for each pixel in the hyperspectral cube. This requires knowing in advance the elements of external orientation (GPS and IMU data) for each line of the hyperspectral cube. The parametric process begins with an estimate of the theoretical view vector ( $\vec{L}$ ) which is the imaginary line of sight to the current pixel, oriented from a horizontal platform facing north. This vector must be turned in three dimensions to get the effective view vector ( $\vec{L}_t$ ) [80]:

$$\vec{L}_t = K * \Omega * \Phi * \vec{L} \quad (2)$$

where K,  $\Omega$  and  $\Phi$  are the coordinate transformation matrices for roll, pitch and true heading, respectively.

Data preparation for parametric geocoding includes adapting the format of the data received to the system. Before arranging spectral lines in a raw hyperspectral cube, mean data are created on insolation (data written using the aerial), and the coefficients of reflectance and subtracting the dark current are calculated.

The data are finally converted to create a visual pyramids in BSQ format with ENVI heading, which allows direct reading of the raw hyperspectral cube in the PARGE programme for parametric geocoding. These operations are carried out automatically, with code written in the Matlab development environment specifically for this purpose. Next, data is synchronised with iMAR (INU) and recording so that the corresponding orientation elements for each image are found using interpolation of linear and angle orientation elements (GPS and INU data), and correspond to the moment when each image was taken (Figure 7). This process is also fully automated with code written in the C # development environment. This means that only data recorded during the system operation, using its frequency, are recorded, while the rest of the big data from iMAR is discarded as superfluous and does not overload the computer resources. The programme can be used, in addition to interpolation, to acquire data in a format adapted to PARGE parametric geocoding. Because of the mutual independence of data groups (images, metadata on images, and data from GPD and INU), and the different programmes used to access them, this kind of configuration allows parallel processing on multi-core systems, which speeds up overall data processing considerable. So, for example, processing a sequence consisting of 1,200 continuous samples, each in 95 spectrum channels, takes about eight minutes.

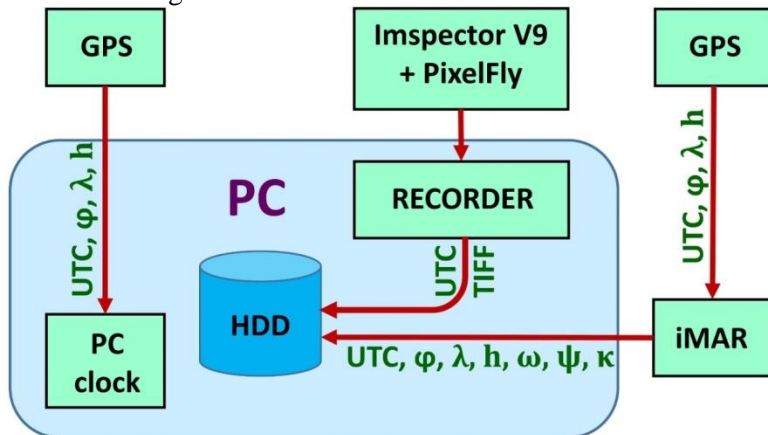


**Figure 7:** Schematic view of the integrated hyperspectral imaging system comprising ImSpector V9 + PixelFly camera.

## Geotagging and Mosaicking Images

The AIDSS multi-sensor imaging system includes multiple sensors integrated onto the same substrate forming a single multi-sensor platform but does not provide the known consistent physical relationship between the multiple sensors. However, it ensures synchronization of all sensors and computers guiding them, and so links the storage times of individual images with IMU and GPS data. Based on these data, geotagging [81] and parametric geocoding [80] can be performed. Geotagging enables the centre of the aerial image acquired by the camera to be linked to the position on the map of the nadir position of the helicopter or RPAS at the moment when the image was acquired. Geotagged images are represented by small icons (small cameras) on the map viewer, and after clicking (in Global Mapper software) on the icon (Figure 8 a), the selected aerial image appears on the screen in full resolution. Note that the image is not geocoded; its top side is oriented in the direction of the flight (not north). The mine scene interpreter can then conduct triage on the geotagged raw images. It is important to emphasize that raw images are interpreted, because using orthography procedures on hilly, mountainous terrain (where there are great differences in elevation) can lead to geometric deformities on the images, making high quality interpretation impossible. In addition, triage is carried by inspecting raw images and selecting those where IMPs have been detected (Figure 8 b). If IMPs are detected on several neighboring images, mosaicking is performed. After that, the selected images and mosaics must be geocoded in order to locate the IMPs in space, and so that images from different sensors can be co-registered. It should be emphasized that this module is not intended for photogrammetric surveys or planning, and the image collection is not always conducted so as to satisfy the strictest geometric conditions for their use (ensuring longitudinal overlaps greater than 60%, or transversal overlaps greater than 20%). However, it is still possible to mosaic the images and geocode the mosaics. The technical characteristics of the current sensors in the module allow sufficient overlap for photogrammetric surveys (particularly with a flight height of over 500 m), but this is not a priority in conducting aerial non-technical surveys for

humanitarian mine action purposes. A further problem in geocoding gathered images is the impossibility of setting ground control points (GCP) within an SHA which is dangerous, or where entry is prohibited. The problems of small longitudinal and transversal overlaps on images and the lack of GCP are resolved using a feature-matching algorithm of Structure-from-Motion (SfM), and this will be explained in the next section.

Image mosaics can be produced and geocoded manually and automatically. Manual geocoding of image mosaics was done from 2001-2005 for the ARC and SMART projects. Mosaics were produced for individual parts of the SHA to give a better picture of the overall scene. The imaging routes were not straight or parallel lines, and the longitudinal and transversal overlaps were insufficient to produce photogrammetric models and mosaics. The first step consisted of joining images on the basis of identical points on them. The second step was to geocode the image mosaic on the basis of GCPs selected on a digital orthophoto map and raw images. Mosaics were produced and geocoded manually using the Descartes (Bentley, USA) software package with Thin Plate Spline transformation [82]. Since 2012, geocoding of image mosaics has been performed using automatically or parametrically specialized PhotoScan (AgriSoft Metashape, Russia) software for visible, multispectral or thermal imagery or ENVI (Harris Geospatial Solutions, Inc, USA) for hyperspectral cubes. Digital orthophoto maps are the best reference for manual geocoding of images or mosaics of images. Their main application is in photo ecometrics of various indicators in an SHA, where ground control is neither available nor needed, and where directly georeferenced digital imagery is acquired to solve the exterior orientation problem [22]. However, if necessary, georeferencing can be performed without in situ GCP [83].

Digital image mosaics and digital surface models (DSM) are produced using a feature-matching algorithm of Structure-from-Motion (SfM) that analyses all images of the aerial data set and searches for matching points. An overview of SfM photogrammetry concept was given in [84]. PhotoScan Professional (Agisoft, Russia) uses this concept and was selected

for geocoding the images and image mosaics of matrix cameras. While working with it, PhotoScan proved to be robust software and less demanding in terms of entering parameters for a photographic survey. All the subsequent procedures for producing the image mosaic were conducted without significant difficulties. After the selected chunk of images was imported into Photoscan Professional, the algorithm detected and matched the identical features on each image. Using these matches, it performed a bundle adjustment to estimate the camera positions and orientations at the time of recording. The geometry of the scene was created by applying a dense, multiview stereo reconstruction to the aligned images, based on this information. To improve the absolute spatial accuracy of the image mosaics, GCP was manually distributed within the imagery. In this system, the information from GPS and IMU was used to perform aerial triangulation without classic GCPs marked on the ground. Small details were selected for GCPs, which were visible on the digital orthophoto map and raw images. Photoscan Professional provided an interface to mark the location of a GCP on each image and its location was then automatically marked on all the images where this GCP appeared.

### Image Quality Assessment

The interpretability of images is determined objectively and subjectively. Based on the parameters of the camera (image resolution, pixel size, focal length) and flight height, the theoretical values of the GSD can be calculated, according to [85] as:

$$M_b = \frac{1}{m_b} = \frac{f}{h} \quad (3)$$

where  $M_b$  is the scale of the image,  $m_b$  the scale denominator,  $f$  the focal length and  $h$  the flight height, or [85]:

$$\frac{s}{f} = \frac{S}{h} \quad (4)$$

where  $s$  is the sensor size and  $S$  the size of the scanned scene, and [86]:

$$GSD = pel * m_b \quad (5)$$

where  $pel$  is the pixel size. With the known GSD and number of pixels in the sensor, the swat can be calculated. This is the value used when planning a mission, and after images have been taken, using calibration markers, the actual value of GSD from the height from which data acquisition took place is determined.

A subjective assessment of the usability of images is done by an experienced scene interpreter, by visually reviewing the images with the use of contextual data. Therefore, a robust method is needed to allow an objective evaluation of the image quality which will correlate well with a visual, subjective judgement. For the objective determination of the interpretability of images, the Image Quality Measure (IQM) [87] was used, with the Johnson criteria. The IQM method is based on an analysis of image spectral density. Based on IQM values, NIIRS values are calculated, which provide the measure of interpretability, or usability. The image quality is described by creating a National Image Interpretability Rating Scales (NIIRS), [88] scale (based on an analysis of the interpreter's results), ranging from 1 (an image with the lowest interpretative quality) to 9 (an image with the highest interpretative quality). This has been used for over 20 years in the surveillance community (it was developed for military purposes) and was later adapted for civilian needs [89]. The method is not standard or developed for all types of objects for civilian use but gives a widely accepted assessment of the usability of images. The Johnson criteria, initially formulated as a method of predicting the probability of target discrimination, were created in 1958 [90]. The model uses the synergy of knowing the origin of how the image was created in the sensor and the interpreter's experience and has been analysed in detail in [91]. Johnson characterized the probability of detecting an object based on its actual resolution in the image. The concept has been substantiated by its own findings. He found that as the number of resolvable cycles across a target increased, so did the probability of an observer successfully locate a target. The Johnson criteria

are the number of line pairs across a target needed for a group of observers to have a 50% possibility of discriminating the (target) object. From 1958 up to the present, this prediction and metrics model has been improved, though there is still no model that accurately predicts target detection in all inclement weather situations [91]. However, the method was used in AIDSS only to assess interpretability before visually interpreting the images, done by human interpreters, who make final decisions on target discrimination. That is, they determine the height level of recording in order to ensure the necessary size of GSD for the detection, recognition or identification of objects of interest with certain sensors by human interpreters.

Measuring positional errors in geocoded and/or georeferenced images or mosaics is difficult in these cases. This is because the places where data are stored are inaccessible (SHAs or other crisis areas), and some scenes have changed drastically, so it is difficult to find the same points in the terrain before and after a crisis situation (for example, the munitions depot in Padjene before and after the fire, explosion and clearance). However, even in such situations, it proved possible to find a certain number of control points on the basis of which accuracy estimates were conducted for the operations implemented. For the orthomosaic, the positional error of these points was measured. The Root Mean Square Error (RMSE) was computed between check point coordinates determined on digital orthophoto and coordinates retrieved from georeferenced image mosaics, to assess the overall spatial accuracy of each dataset.

Before using and processing hyperspectral imagery, rigorous pre-processing steps were undertaken to ensure the quality, accuracy and interoperability of the data used. After parametric geocoding of hyperspectral data acquired using a V9 ImSpector line scanner, sensor radiance performance was inspected and validated. We used a calibration procedure based on the Supervised Vicarious Calibration method [92] which included: (I) Quality assurance of radiometric information, (II) Stability and general performance analysis, (III) Radiometric calibration and (IV) Atmospheric calibration.

In the quality assurance procedure, MODTRAN was used to reconstruct the atmosphere above selected targets with ground-truth measured reflectance, and then compare the results with the obtained at-sensor radiance [93]. Two indices - Rad/Ref (at-sensor Radiance divided by ground truth Reflectance) and RRDF (Radiance to Reflectance difference factor) indices were used to spot faulty performance of the sensor prior to the next data processing stages.

In the present study, reflectance-based vicarious calibration was used for radiometric recalibration, as the image at-sensor radiometric data were calibrated by comparison against the modelled at-sensor radiance based on the in situ measured reflectance of the selected, well-defined ground targets. The simplest, fastest method for atmospheric correction is the Empirical Line Method (ELM). It uses a set of ground targets of known reflectance to derive a relationship between sensor-spectral radiance and scene-spectral reflectance. ELM assumes that the radiance image contains some pixels with a known reflectance spectrum, and also that the radiance and reflectance values for each wavelength of the sensor are linearly related. Therefore, the image can be converted to reflectance by applying a simple gain and offset derived from the known pixels.

The at-sensor measured radiance is given in an equation for each wavelength:

$$L_s = \frac{\tau\rho E_0}{\pi} + L_{\text{path}} \quad (6)$$

where  $E_0$  is the sun's radiance above the atmosphere at a certain zenith angle,  $\tau$  is the atmospheric transmittance,  $\rho$  is the surface reflectance and  $L_{\text{path}}$  is the selective scattering (Rayleigh and Mie) contribution to the sensor output [92]. Assuming that during the operation, the sensor keeps the calibration coefficients that were generated in the laboratory during the system calibration stage, equation (6) is valid as it stands. In the case of a non-calibrated sensor (or divergence from the laboratory calibration), the achieved at-sensor radiance ( $L_s$ ) is a product of the real radiance multiplied by gain and offset coefficients that

adjust the mis-calibrated laboratory information to at-sensor radiance as follows:

$$L_s = [L_{(\text{gain})} \left( \frac{\tau \rho E_0}{\pi} + L_{(\text{path})} \right)] + L_{(\text{offset})} \quad (7)$$

where  $L_{(\text{offset})}$  is the unknown noise that has entered the sensor since the time of the last laboratory calibration and  $L_{(\text{gain})}$  is a amplification factor that depends on the sensor's functionality and surrounding conditions that diverges from the laboratory calibration process [92].

## Laboratory and Terrestrial Field Hyperspectral Imaging System Design

The ImSpector V9 hyperspectral line scanner (HSLS) was combined with a PixelFly monochrome area camera to form the Imaging Spectrograph System, or geometric sensor model (Figure 8).

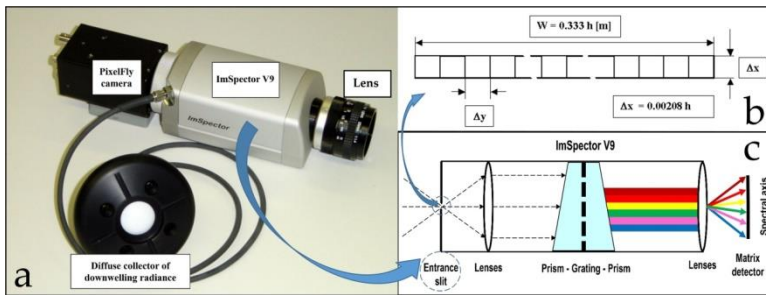


**Figure 8:** a) ImSpector V9 hyperspectral line scanner with diffuse collector to measure incident down-welling irradiance (connected to the V9 head via fiberoptic cable) and PixelFly matrix camera. b) ImSpector V9 sensor geometry mapping scheme. c) Operating principle of ImSpector V9.

The ImSpector V9 (Figure 8a) employs a direct sight (on-axis) optical configuration and a volume type holographic transmission grating. This grating is used in a patented prism-grating-prism construction (PGP element, Figure 9) which provides high diffraction efficiency and good spectral linearity [94]. It is almost free of geometrical aberrations due to the on-

axis operation, and independent of incoming light polarization due to the use of transmission optics only [94]. The robust structure of the ImSpector V9 suits both industrial and scientific applications that require rapid, precise spectral measurements at low cost. The spectral resolution of the spectrograph depends on the width of the entrance slit and linear dispersion produced by the spectrograph optics. The minimum limit for the spectral resolution is set by the imaging capability of the optics. The configuration which we used consisted of the optical system with focal length of 23 mm (Schneider Kreuznach Xenoplan 1.4/23) and narrow slit 8.8 mm long and 50  $\mu\text{m}$  wide (Table 3), which enables spectral resolution of 4.4 nm for 95 channels in a spectral range from 430 nm to 900 nm (Figure 8b, Table 3). At the nadir, the system provides imaging of a narrow strip measuring  $(0.333 \times h) \times (0.00208 \times h)$ , where  $h$  denotes height above the sample (or ground) (Figure 8c).

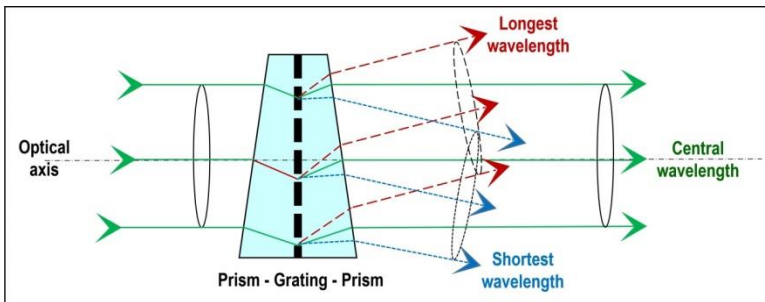


**Figure 9:** Basic principle of the direct-vision PGP element.

PixelFly camera was chosen because the CCD sensor records the light information for each pixel as a grey level with 12-bit dynamic range. Although camera control software enables to convert the 12-bit data of each pixel to 8-bit triplet ( $P_{\text{RED}}$ ,  $P_{\text{GREEN}}$ ,  $P_{\text{BLUE}}$ ) [47], this capability was not used to produce hyperspectral images. After the assembling procedure, the PixelFly camera and ImSpector V9 need to be aligned so that the spatial axis of the spectrograph is parallel to the horizontal pixel lines of the camera.

**Table 3:** Basic specifications of ImSpector V9 line scanner [94] and PixelFly area CCD camera [78].

ImSpector V9 specifications		
Spectral range	430 – 900 nm $\pm$ 5 nm	Designed for 6.6 mm detector; corresponding to shorter axis of 2/3" CCD
Spectral	4.4 nm	With 50 $\mu$ m slit
Numerical	0.18	F/2.8
Slit width	50 $\mu$ m	
Effective slit	8.8 mm	
Image size	6.6 mm $\times$ 8.8 mm	Corresponding to standard 2/3" CCD
Magnification of spectrograph optics	1x	
PixelFly basic specifications		
Image	1280 $\times$ 1024 pixels	
Pixel size	6.7 $\mu$ m $\times$ 6.7 $\mu$ m	
Scan area	6.9 mm $\times$ 8.6 mm	
Imaging frequency (frame rate)	12.5 fps	At binning with factors 1
	24 fps	At binning with factors 2
Pixel scan rate	20 MHz	
Exposure time	10 $\mu$ sec – 10 sec	
Binning horizontal: Binning	factor 1, factor 2 factor 1, factor 2	

The sun shines at elevation angle  $\theta$  measured from the horizontal axis. Waves reflected from the ground surface are collected at the nadir by an optical lens and receiving pattern diagram  $F(\theta)$ . Incident waves are collected by a diffuse collector with a receiving pattern diagram  $F(\alpha)$  (Figure 10a). Other characteristics of the camera include the horizontal and vertical binning capability. Horizontal binning determines the cross-track width of the image, while vertical binning determines the number of spectral bands. The horizontal axis (1280 or 640 pixels) presents the spatial axis and calibrating part, while the vertical axis (1024 or 512 pixels) presents wavelengths from 430

nm to 900 nm (Figure 10a, Table 4). The dimensions of the analyzed area below the HSLs in static mode (no movement) were defined (Figure 10b). The HSLs output was  $1280 \times 1024$  pixels (or  $640 \times 512$  pixels), whereas  $1170 \times 1024$  or  $585 \times 512$  pixels represent 12-bit intensity of the reflected waves (Figure 10c),  $110 \times 512$  or  $55 \times 512$  pixels on the right side of the image contain information about incident waves (Figure 10c). The horizontal axis  $x$  is a spatial axis with width  $W$  and contains 1170 or 585 pixels. For the acquired area, the HSLs V9 and PixelFly digital area camera produce from 12.5 (binning factor combinations: H1-V1 and H1-V2) to 24 (binning factor combinations: H2-V1 and H2-V2) images per second, each with  $1280 \times 1024$  pixels (factors 1) or  $640 \times 512$  pixels (factors 2). The vertical axis  $\lambda$  present wavelengths in a range from 430 to 900 nm. The ratio of reflected  $E_{ref}$  and incident  $E_{inc}$  value at wavelength  $\lambda_i$  is the measure of the reflectivity at this wavelength (Figure 10b). The HSLs V9 and image parameters are managed using *Recorder* software, which was written entirely in C++ language as part of the ARC project. Recorder is an application that actually controls the HSLs V9 (exposure time and horizontal binning factors) and performs image acquisition (Figure 10c and d). The control parameters for the HSLs such as exposure time, horizontal and vertical binning factors and image depth can be set before image acquisition via the Recorder interface (Figure 10c and d).

**Table 4:** Horizontal and vertical binning factors, image width and number of spectral bands of line images that can be captured at one time for all horizontal and vertical binning combinations of the HSLs.

Horizontal binning factors	Vertical binning factors	Image width (pixels)	Spectral bands
1	1	1280	1024
1	2	1280	512
2	1	640	1024
2	2	640	512

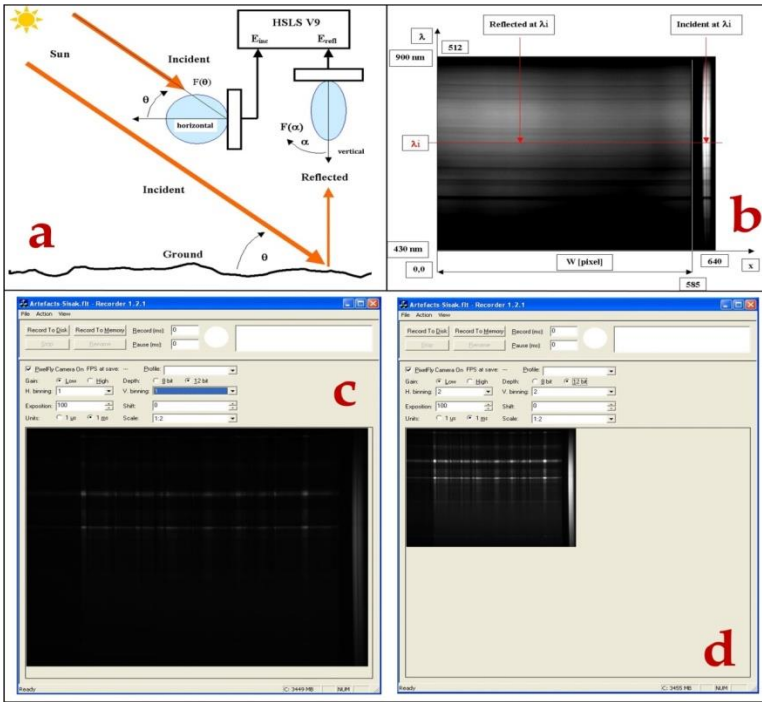


**Figure 10:** a) Geometry in the vertical plane of measurements with the HSLs V9 (picture courtesy of M. Bajić). b) Output images from the HSLs V9 and PixelFly digital area camera in a spectral range from 430 to 900 nm. Left:  $585 \times 512$  (reflected) pixels present 8-bit intensity of reflected waves. Right:  $55 \times 512$  (incident) pixels at the right side of the image contain information on incident waves in binning II configuration. Recorder interface for: c) binning with factors 1 and d) binning with factors 2.

Values  $E_{inc}$  and  $E_{ref}$  measured by the HSLs V9 enable calculation of the reflection coefficient  $r$  according to the relation (8):

$$r = \frac{\frac{G_{ref} - E_{ref}}{F(\alpha)}}{\frac{G_{inc} - E_{inc}}{F(\theta)}} \quad (8)$$

where the pattern diagram of the HSLs V9 is  $F(\theta)$ , and of the diffuse collector  $F(\alpha)$ ; the gains (if other than 1)  $G_{inc}$ ,  $G_{ref}$  are of the bands for measuring  $E_{inc}$  and  $E_{ref}$ . Thus, we did not measure radiance but calculated the reflection coefficient according to the actual measurements of the reflected and incident portions of the

electromagnetic spectrum. The reflection coefficient is the ratio of the amount of electromagnetic radiation recorded by the sensor ( $E_{ref}$ ) to the amount of electromagnetic radiation recorded by diffuse collector near the sensor ( $E_{inc}$ ). It is a property of the observed material and is equivalent under different illumination conditions.

Since this hyperspectral imaging system was designed for airborne remote sensing applications, it also consists of a subsystem for navigation, position determination and orientation of the system in space. This subsystem consists of a single-frequency GPS device integrated with an inertial measurement unit (IMU) iVRU-RSSC by iMAR GmbH with a working rate of 200 Hz, and additional GPS units arranged in or on the platform. iVRU-RSSC is a triple-axis inertial system with three mutually perpendicular MIL-MEMS gyroscopes used to determine the angle elements of the spatial orientation of the sensor, and 3 MEMS accelerometers used to determine the acceleration components along all three axes. This six-degree-of-freedom measurement unit provides accurate and instantaneous positional data at a high sampling rate, which is continuously recorded during surveying and synchronized with image data (spectral lines). Thus, if it would be necessary to define the precise position of certain spectral data in space, the subsystem could be activated to collect the required data to execute parametric georeferencing. Although the subsystem was not used to collect the spectral data presented later in this paper, but the system has this functionality and could be applied in possible future applications like e.g. mobile hyperspectral mapping.

## Sensor Bracket and Control System

For the purpose of terrestrial recording within the TIRAMISU project (2012), a sensor bracket and control system were built. An aluminium construction with a 3-metre guide-rail was made (Figure 11), along which the HSL V9 could move and collect spectral samples continuously. The source of light used during imaging in the laboratory was a halogen lamp, which due to its smooth spectral properties, had no significant peaks over the entire visible and NIR spectra. To enable movement and

manipulation while collecting spectral samples in succession, a control system with an engine and software was designed (Figure 12). Each time the programme started (including charging), initialization and alignment of the system were carried out by selecting *Init.* This sub-programme (yellow number 1 on Figure 12) gives the command to place the system at the zero point on axis X, the starting point (far left margin) on the guide, from the perspective of the operator). The maximum distance from zero to the farthest point is  $x = 2,450$  mm, and the speed ranges from 1 to 200 mm/s. The software enables the following recording regimes:

- Continual movement and collection of spectral samples at a given speed to the given position
- Movement at the given speed by sections of the route, stopping at positions where spectral samples are collected

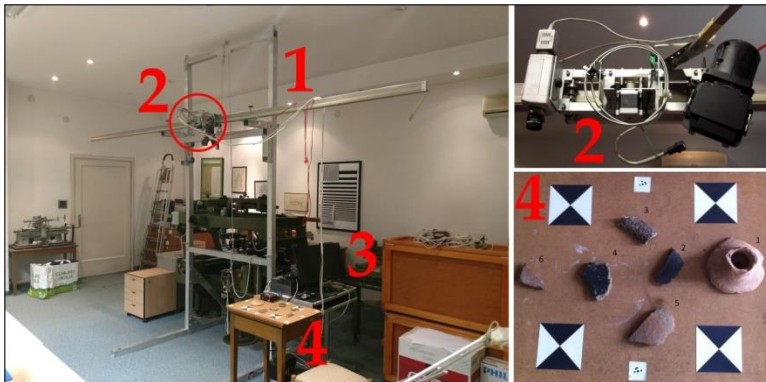


**Figure 11:** 1) Sensor bracket; 2) HSLV V9, diffuse collector, halogen lamp, engine (in red circle), 3) control system (industrial controller and motor controller) and 4) table with Roman archaeological artefacts found in Sisak, Croatia [95].

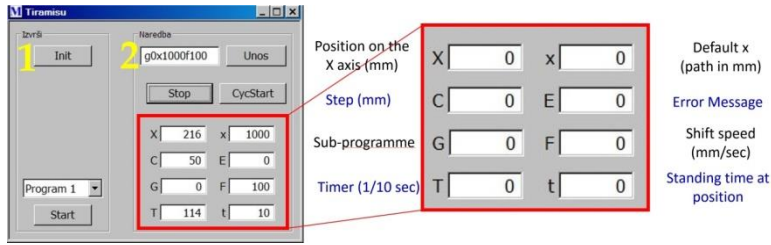


**Figure 12:** Software interface display of control system for collecting data and variable parameters.

## Spatial Calibration and Modulation Transfer Function

Hyperspectral sensors used in close-range imaging applications are primarily calibrated in the spectral domain, while their spatial calibration is questionable or not implemented at all. To (geo)locate the spectral information gathered by the HSLs V9 sensor, a mathematical model of the imaging of the scene to the image plane was derived and implemented, taking into consideration the expected systematic errors that influence measurement results. A detailed description of the applied 2D method can be found in [50]. In brief, it features an algorithm which rests on the theory of the central projection of each point in space in the image plane, using a collinearity equations. This mathematical model is the standard one used when calibrating cameras with array sensors for photogrammetric purposes. In this case, the central projection of a point in space was used in a two-dimensional image plane, and with a line scanner there is only one dimension, so a mathematical model was set up and resolved so that the image coordinate system was reduced to only one dimension [49]. Hyperspectral measurement by the HSLs V9 was performed along the line of the black and white sample with the repetitive crown pattern target surface (Figure 13). When calibrating the line scanner to the given sample, the aim was for the line of recording to pass along the line joining the centre of edge markers A and B, with a black-and-white triangular sample (Figure 13, red line). Focusing was performed on the basis of visual judgment.

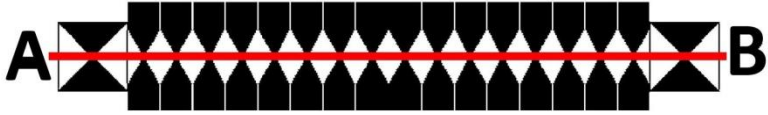


**Figure 13:** Calibration pattern for spectral calibration of HSL5 V9.

MTF is the ratio of output modulation (sinusoid wave) to input modulation (square wave) (10) normalized to unity at zero frequency, while modulation is the variation ( $V_{max}$  and  $V_{min}$ ) of a sinusoidal signal about its average value (9) [97]:

$$MODULATION = M = \frac{V_{max}-V_{min}}{V_{max}+V_{min}} \quad (9)$$

$$MTF(f) = \frac{M_{OUTPUT}(f)}{M_{INPUT}(f)} \quad (10)$$

MTF is the magnitude response of the optical system to sinusoids of different spatial frequencies, and a measure of how well a system will faithfully reproduce the input object. An object or image-plane irradiance distribution is composed of spatial frequencies in the same way that a time-domain electrical signal is composed of various frequencies - by means of a Fourier analysis. By taking a one-dimensional profile across a two-dimensional irradiance distribution, we obtain an irradiance-vs-position waveform, which can be Fourier decomposed in exactly the same way as if the waveform was in the more familiar form of volts vs time [51]. There are two general methods of determining MTF. The direct method is based on measuring the response of the sinusoidal signals of the decreasing bar widths on the recorded template. The indirect method is based on calculating Fourier's transformation of linear transference function. We used the direct method approach as a handy reality check, comparing a measured spot size to calculated MTF values. The target for measuring and calculating MTF was the binary pattern of black and white pairs of decreasing bar widths that simulated different object sizes, as seen in Figure 7a, which was easy to make [49]. The increase factor of the black-and-white bars was  $2^{1/6}$  [97], which means the width of pairs was calculated as between 20.88 mm (widest) and 0.92 mm (narrowest).

The calculation of MTF at any particular frequency requires that a CTF calculation (11) is made at a series of frequencies harmonically related to the desired frequency of the MTF measurement.

$$CTF = \frac{I_{max}-I_{min}}{I_{max}+I_{min}} \quad (11)$$

where  $I$  is the average intensity of black ( $I_{min}$ ) and white ( $I_{max}$ ) bars. For an infinite square wave, CTF is defined as the image modulation depth as a function of spatial frequency. Series conversion between CTF (12) and MTF (13) using Fourier decomposition of the square waves, can be derived thus [51]

$$(f_x) = \frac{\pi}{4} \times \left| MTF(f_x) + \frac{MTF(3 \times f_x)}{3} - \frac{MTF(5 \times f_x)}{5} + \frac{MTF(7 \times f_x)}{7} + \frac{MTF(11 \times f_x)}{11} \right| \quad (12)$$

and

$$MTF(f_x) = \frac{\pi}{4} \times \left| CTF(f_x) + \frac{CTF(3 \times f_x)}{3} - \frac{CTF(5 \times f_x)}{5} + \frac{CTF(7 \times f_x)}{7} + \frac{CTF(11 \times f_x)}{11} \right| \quad (13)$$

This operation must be repeated for each frequency at which we want to find MTF. Typically, CTF need to be measured at enough frequencies to plot a smooth curve, and then interpolated to find the CTFs at the frequencies needed to compute an MTF curve from the CTF data. It is generally not sufficiently accurate to take only the CTF measurements as MTF measurements (Figure 14b), but this can be a good estimate of MTF behaviour [51].

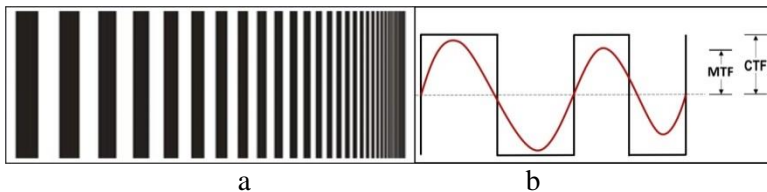


**Figure 14:** a) Template with striped black and white bars of decreasing width. b) Components of CTF and MTF. CTF is usually equal to or greater than MTF.

## Creating a hyperspectral cube

The spatial accuracy of continuous measurements depends on the movements of the system. When the system is on a moving platform, the ground can be scanned linearly at line intervals  $\Delta s$  and  $GSD_v$  along the line. Line interval  $\Delta s$  depends on the velocity of the system  $v$  and frequency of storing images  $f_s$  in the acquisition system. To use the line scanner in full imaging mode (acquiring contiguous scan lines), it is necessary to find the optimum speed of the HSLs V9. It is a function of the required GSD and scanner imaging frequency, according to a simple equation (14), used to arrive at optimum distance per second (according to Šemanjski et al., [46]):

$$S = \frac{GSD}{f_i} \quad (14)$$

where:

- $S$  = Speed of the HSLs V9 (m/s),
- $GSD$  = Ground Sampling Distance across the line scanner (m) and
- $f_i$  = Imaging scan period (s).

The maximum frame rate per second was around 24 Hz and depended on radiometric parameters during the collection of reflected radiation. The HSLs V9 requires a very complex calibration procedure and time-consuming processing. Software solutions were also developed to produce a raw hyperspectral cube (merging a large number of continuous line samples in a two-dimensional image without georeferencing) in the Matlab software package. These operations were automated, with code written in the Matlab development environment specifically for this purpose, and contained the following procedures:

- Exporting raw data (linear images) and transforming them into TIF format in Recorder programme
- Creating mean data on insolation collected with the diffuse collector, along each line
- Calculating the reflectivity coefficient

- Correcting the spectral responses with dark current data (dark image subtraction)
- Stacking spectral lines in the hyperspectral cube.

When creating the hyperspectral cube, we also took into account the appearance of bright pixels at long exposure times due to sensor lattice damage (hot pixels), which can be corrected via dark image subtraction. Hot pixels in the sensor must be corrected by characterizing their behavior as a function of exposure time when they are not exposed to any light. This can be achieved by closing the aperture completely and obtaining several measurements. By obtaining the baseline pixel values for several exposure times, hot pixel background signals can be modelled in each pixel by [51]:

$$h_{bg,ij} = a_{ij} \times T_{exp} + b_{ij} \quad (15)$$

where indices  $i, j$  indicate the pixel's position in the sensor,  $a_{ij}$  and  $b_{ij}$  are the coefficients that model the linear behavior of the pixel as a function of exposure time  $T_{exp}$ , and  $h_{bg,ij}$  is the estimated hot pixel value that should be subtracted from each pixel for every new measurement. The data are finally converted to create a pyramid in BSQ formation with ENVI header. Thus, it is possible to download the raw hyperspectral cube directly in PARGE 2.3 software, in which parametric georeferencing is carried out [79] of the hyperspectral cube.

The procedure for parametric georeferencing involved adding the exact spatial position of each pixel in the hyperspectral cube. This procedure required in advance the given elements of external orientation (GPS and IMU data) for each line in the cube. During data collection, Recorder software along with spectral lines created a table in which the GPS and IMU data were linked with each stored line. Thus, the fine synchronization of images and metadata necessary for the parametric georeferencing of the hyperspectral cube could be performed. This procedure was also fully automated by applying the script in C# programming language. Only data recorded during the scanner operation at its frequency were used, while the rest of the considerable data from iMAR were rejected as unnecessary,

in order not to overload the computer resources. Using this programme, apart from interpolation, the data can be acquired in a format adapted to the PARGE parametric geocoding programme. Due to the mutually independent data groups (linear images with the HSLs, their metadata and data from IMU), and various programmes used to access them (Matlab and C#), this configuration allows parallel processing on multi-core systems, which speeds up the overall data processing chain considerably. A detailed description and explanation of the parameter georeferencing process can be found in [80].

## Results of the AIDSS Module for Aerial Data Acquisition

The results of this AIDSS module were images with various sensors and discernibility, geotagged images (Figure 15a), and GPS and IMU data which were necessary to place the images in space and create the orthomosaic (Figure 15a). In the next section, just some of the results of the module are shown, to illustrate the potential it represents for data acquisition at the scenes listed in 2.1.

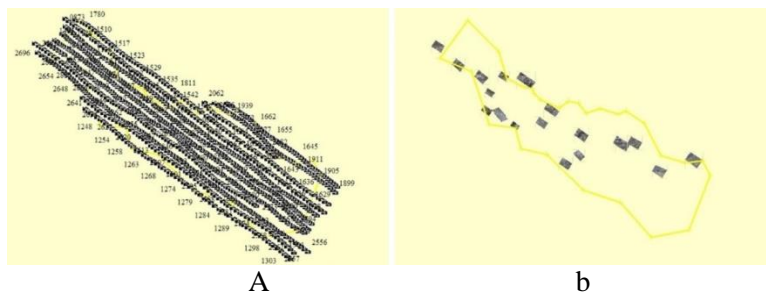


**Figure 15:** Examples of depictions of a) geotagged images and b) extracted and georeferenced images, after triage, which contain IMPs in one SHA (yellow polygon).

## Sensor Pods

Sensor pods were designed and made especially for each individual platform. For the Mi-8 and Bell-206 helicopters (Figure 16a), two types of large aerodynamic sensor pods were

made (weighing over 20 kg), since there was no issue with the payload on these platforms. The difference was only in the bearing supports installed on the platforms. For the Gazela helicopter, there was also no restriction in terms of the payload, and this helicopter has an opening in the floor, which made the development of the sensor system easier (Figure 16c).

For the RPAS platform, smaller sensor pods were designed and made, depending on their payloads (the weight of the system varied from 3.5 to 5 kg, Figure 16d). Micro computers were built into these sensor pods so that the sensors could be activated remotely from the ground.

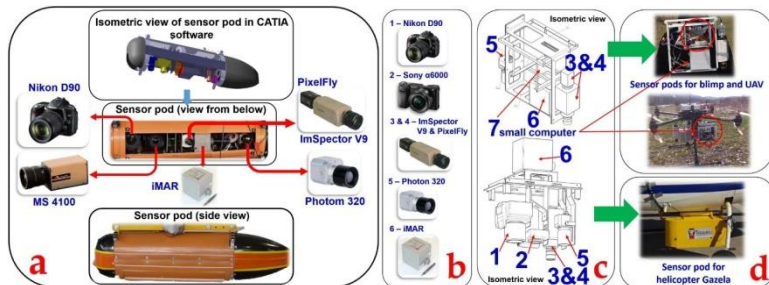


**Figure 16:** a) Example of the first sensor pod designed and made with associated sensors for the Mi-8 and Bell-206 platforms, b) sensor used; c) examples of a sensor pod designed and made for UAV and blimp platforms (top), and helicopter Gazela bottom) with associated sensors.

### Analysis Vibration of the Sensor Pod Installed on the Mi-8 Helicopter

Experience with different aerial platforms (Bell-206, Mi-8, and Gazela helicopters, RPAS Fenix fixed-wing, and several multirotor UAVs) used for airborne imagery acquisition has shown that sensor vibration is the main cause of image blurring. There are no published data about the vibration of these aerial platforms. This fact motivated us to analyse the vibration which occurred in a pod containing electro optical sensors. We selected the pod installed underneath the Mi-8 helicopter. Data on vibrations were collected using the inertial positioning system (iMAR), along with data provided by the GPS receiver. By analysing the collected acceleration in flight direction X, in a left

or right direction Y and in a vertical direction Z, we were able to identify several flight phases: a) engines on, helicopter on the ground, b) take-off, helicopter climbing, and c) the stationary phase of the helicopter's flight. Since only the stationary parts of the flight route were usable for image acquisition, the spectral analysis of vibration was carried out on segments of this phase (Figure 17a and b). The results obtained, shown in Figure 17c-e, enabled the design, development and implementation of passive vibration damping to decrease image blurring.

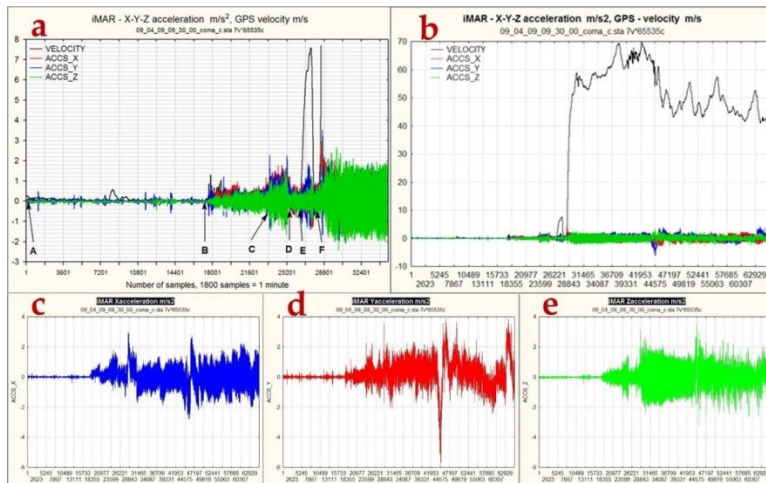


**Figure 16:** a) Vibration phases: AB engines off, BCD engines on, EF increase power and take off, > F flight; b) the diagram shows the speed (velocity, m/s) and acceleration dependence on the X, Y and Z axes (ACCS\_X, ACCS\_Y, ACCS\_Z, m/s<sup>2</sup>) in relation to the number of samples. Speed was calculated based on data from the GPS receiver with a frequency of 1 Hz, and acceleration was read from iMAR with a frequency of 20 Hz on the measured platform accelerations per axis: c) X axis, d) Y axis and e) Z axis.

The analysis of spectral density of the power of vibration showed that vibration occurred at the following frequencies: ~3.2 Hz, ~4.0 Hz and ~7.5 Hz. The first is the direct frequency caused by the rotation of the main rotor (without blades). The second is the frequency caused by aliasing vibration at 16 Hz, which is the result of the rotation at 3.2 Hz of the five blades of the main rotor depicted in reverse under 10 Hz ; 16 Hz – 10 Hz = 6 Hz, which is shown counting down from 10 Hz and gives ~4 Hz. The

last is the actual frequency of vibration or occurs due to aliasing wrongly depicted frequencies  $\sim 12.5$  Hz, for unknown reasons. Based on these measures and the results of the analysis, passive dampers were designed for 3.2 Hz, 16 Hz, 7.5 Hz and 12.5 Hz using Enidine vibration insulators, Figure 18.

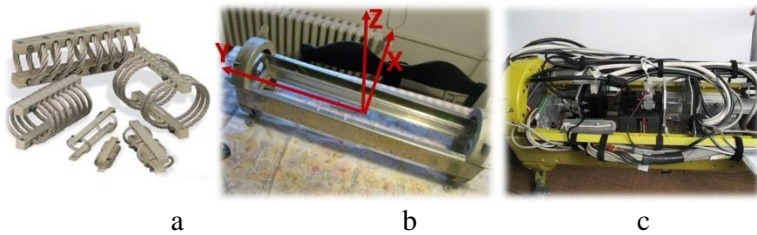


**Figure 18:** a) Wire rope vibration dampers [98], b) coordinate axes in sensor pod, c) wire rope dampers installed in the sensor pod.

During the 2010 AIDSS mission in Bosnia and Herzegovina, tests were conducted (to reduce the colour blurring in images after passive vibration damping), in which Enidine vibration isolators were a) blocked (no vibration damping), or b) isolators were enabled to damp the vibrations. The images were collected in both cases and excellent results achieved: images with activated isolators could be zoomed seven to eight times before discernible blurring occurred and have larger standard deviation (27.921 without isolators vs 30.906 with isolators, Figure 19). When vibration isolators were disabled, zooming two or three times made the images blurred.

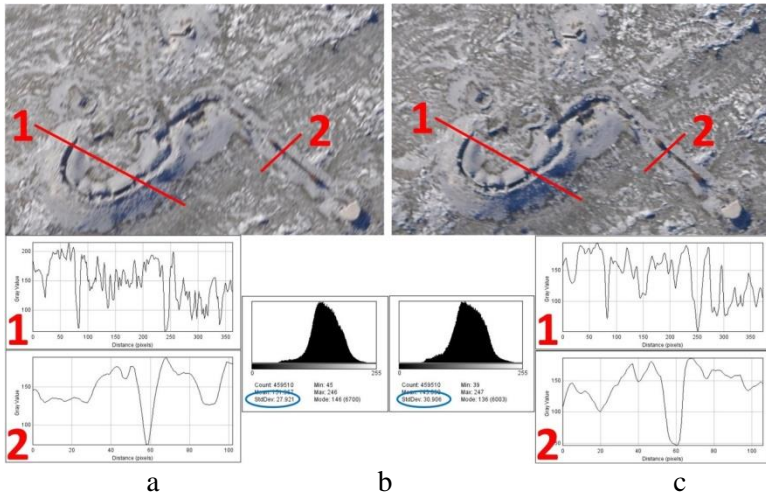


**Figure 19:** a) Images collected without damped vibrations with two profiles over the IMPs (trenches). b) Passive damping of vibrations keeps the image sharper with two profiles over the IMPs (trenches). c) Histograms of images with standard deviations (in blue ellipses).

## Images

Images collected with visible digital cameras had the best GSD and depicted the largest recorded terrain (Figure 20). These images were used to gain a better insight into the situation in the scene and detect IMPs according to geometric characteristics (trenches, bunkers, various types of shelter). Hyperspectral sensor images have poorer GSD than the multispectral sensors (Figure 20a), but they exploit the full spectral dimension, which better reflects the continuous nature of actual spectra. LWIR Photon 320 and THV 1000 sensors also have poorer GSD than the visible digital cameras (Figure 20b), however, they are used to detect IMPs via their thermal characteristics. Detection of strong IMPs is carried out by mine scene interpreters through visual interpretation of images collected with visible digital cameras and LWIR sensors. The methodology for isolating IMPs on hyperspectral images is described in [47].

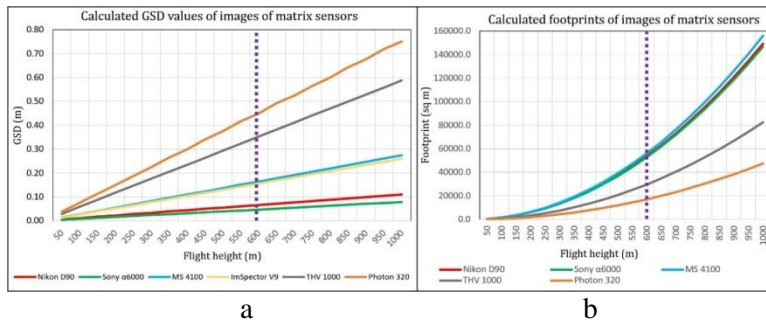


**Figure 20:** a) Theoretical values of GSD of images of more significant AIDSS sensors for flight heights of 50 to 1000 m; b) Theoretical values of image footprints of matrix sensors.

Table 3 shows the confidence values of subjective assessment of identifying IMPs by mine scene interpreters, and an objective assessment of image quality using NIIRS. The values of 5 to 7 on the NIIRS scale (Table 5) allow detection of fortification objects on images taken by selected sensors. Figure 21 shows a diagram comparing the percentage of detection probability, recognition and identification for two strong IMPs (a trench and a bunker) and the GSD which ensures it. The critical value of the trench (its normal width) was determined at 0.6 m, and for the bunker (its normal radius) at 2 m.

**Table 5:** Some examples of radiometric characteristics, theoretical GSD of selected images with IMPs, cameras with which the images were collected and the subjective confidence of the human image interpreter in his findings.

IMP	Sensor	GSD (m)	IQM	NIIRS	Subjective confidence of the human image interpreter
Bunker	MS-4100	0.29	0.00893	5.38	1
Drywall	Nikon D90	0.10	0.00107	5.51	1
Trench					1
Trench	Canon 5D	0.19	0.00913	5,28	1
Battlement					1
Shelter					1
Unexploded ordnance (UXO)	Sony α6000	0.03	0.0595	6.7	1

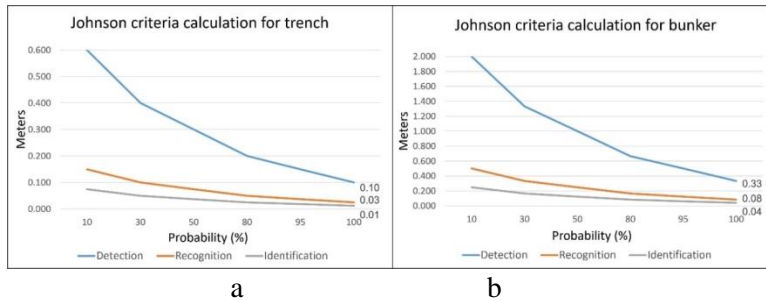


**Figure 21:** GDS size for the detection, recognition and identification of a) a trench and b) a bunker. Both diagrams show the GSD values for 100% detection, recognition and identification of the objects on the image.

### Images from the Milekovići and Vrankovići Sites

Airborne continuous data acquisition was conducted at SHA Milekovići (16 and 23 April 2003) and Vrankovići (28 and 30 April 2003) using these sensors:

- DuncanTech MS-3100,
- Thermovision 1000 FLIR
- ImSpector V9 + PixeFly on a Bell-206platform.

Data acquisition was performed from flight heights of 900, 500, 260 and 130 m in nadir with  $v = 22$  m/s and a south-north flight direction (Table 6). MS3100 was used to acquire 32 GB of VNIR images (blue, green, red, near infrared, 8 bit). At the Milekovići site 18.7 GB, and at the Vrankovići site 13.23 GB of VNIR images were collected, with 100 MB at Milekovići and 75 MB of LWIR images at Vrankovići, and 4 GB of hyperspectral images at Milekovići and 3 GB at Vrankovići (Table 6). During the data acquisition using the multispectral sensor LWIR sensor and hyperspectral sensor at both location, certain problems arose. The main problem was that it was difficult to accommodate to the strong wind which prevented recording on the planned route. Air currents affected the stability of the Bell-206 helicopter in flight, and it had to fly downwind or parallel to the wind, so it was difficult to keep to the planned route (or general direction). Therefore, the recording route had to be adjusted, though it had been planned to economize flight time and the consumption of

various resources, in accordance with the shape of the area of interest for which data acquisition was necessary. Filming of many strips had to be repeated due to wind impact. The next problem was charging the THV 1000 sensor. Due to the low capacity of the power supply, the THV-1000 worked for a shorter time than other sensors. Furthermore, the navigation system (based on GPS) was interrupted due to the small number of satellites. Despite all the problems, very useful results were derived and a better insight into the situation in the SHA was gained. LWIR images at higher altitudes acquired by THV-1000 outside the area in Milekovići showed trenches and bunkers that could not be seen from the ground. These images revealed details not seen on VNIR images, which justified their use in the module. An example can be seen in Figure 22a and b. On the VNIR image inside the Milekovići SHA the top part of the trench was only just showing, while on the LWIR image, it can be seen in its entirety. Airborne continuous data acquisition was performed along with airborne spectral sampling of selected strips in Milekovići using a hyperspectral sensor (ImSpector V9 + PixelFly) (Figure 22c). Spectral sampling using a hyperspectral scanner was carried out in the areas for which mine reports were available, with a high confidence level in their existence, based on MIS data. These data were not visualized but used in large numbers to create a diagram of coefficients of reflectance (Figure 22c). The examples of RGB, VNIR and LWIR images collected of two bunkers and a drywall connecting them in Vrankovići are shown in Figure 15. The Normalized Difference Vegetation Index (NDVI) is also shown and calculated based on the MS 3100 camera channels (Figure 22f).

**Table 6:** Data on airborne continuous data acquisition and images gathered for Milekovići and Vrankovići SHAs

Site / Date	Flight height (m)	Flight direction	Flight speed (m/s)	VNIR Images		LWIR Images		HyperSpectral Images	
				Amount of data (GB)	GSD (m)	Amount of data (MB)	GSD (m)	Amount of data (GB)	GSD (m)
<b>Milekovići</b> 16 and 23 April 2003	130, 260, 500, 900	planned: South-North	20	18.7	0.04, 0.09, 0.16, 0.30	100	0.09, 0.15, 0.30, 0.53	4	0.03, 0.07, 0.13, 0.23
<b>Vrankovići</b> 28 and 30 April 2003	130, 260, 500, 900	planned: South-North	20	13.2	0.04, 0.09, 0.16, 0.30	75	0.09, 0.15, 0.30, 0.53	3	0.03, 0.07, 0.13, 0.23
<b>TOTAL</b>				<b>31.9</b>		<b>175</b>		<b>7</b>	

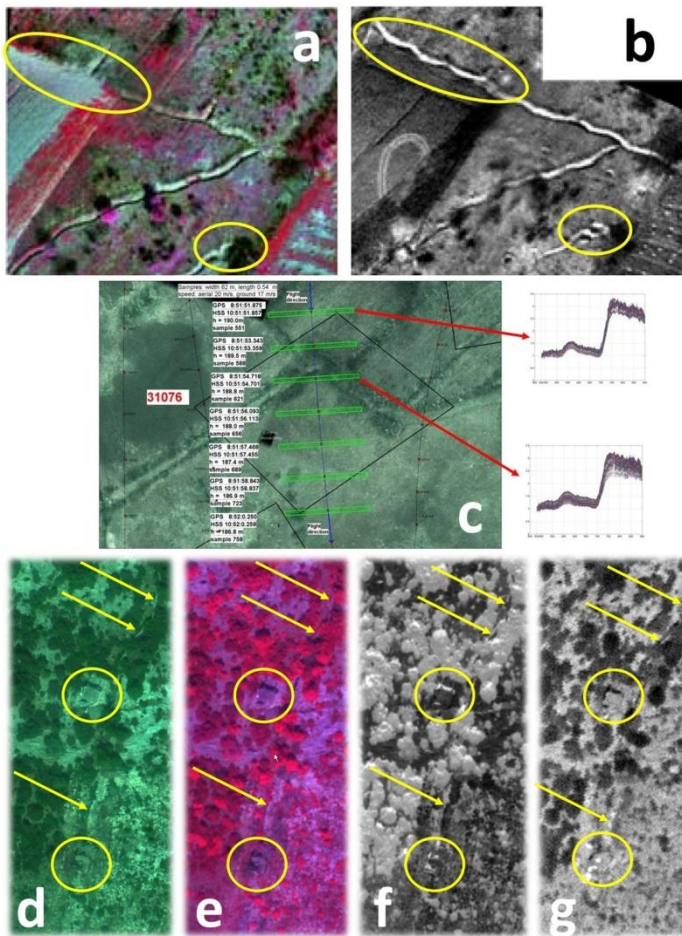


**Figure 22:** Examples of images of part of Milekovići SHA (from a height of 500 m) collected using sensors a) DuncanTech MS3100 (VNIR) and b) Thermovision 1000 FLIR (LWIR) on which trenches can be seen (yellow ellipses). c) Depiction of the position of samples collected using the hyperspectral linear scanner ImSpector + PixelFly and spectral responses of the area scanner. Examples of part of Vrankovići SHA and processed images, on which two bunkers can be seen (yellow circles) and a dry wall connecting them (yellow arrows), d) RGB images by DuncanTech MS3100, e) VNIR image by DuncanTech MS3100, f) NDVI calculated on the basis of DuncanTech MS3100 channel, g) LWIR image by Thermovision 1000 FLIR (LWIR).

## **Imagery from the Gospić, Bilje and Drniš Sites**

During the airborne missions in Gospić, Bilje and Drniš, 54.8 GB of images were acquired using sensors: Canon EOS 5D RGB camera (26 GB), multispectral MS3100 camera (14.8 GB) and LWIR Photon 320 (24 GB) camera. The Canon EOS 5D has a sensor measuring 38.8 \* 23.9 mm, picture resolution of 4368 \* 2912 pixels (effective 12.8 megapixels) and was only used in these missions with a 38mm focal length lens. Data acquisition was carried out from 26 March to 10 April 2009, from the Mi-8 platform, at a speed of 33 m/s and a height above ground of 600 m. The flight directions while gathering data were projected primarily according to the lie of the relief, and then were modified daily according to the weather forecast and wind direction, as necessary. These images and data were collected with the aim of enabling reliable detection of IMPs and IMAs, so for the interpretation, mainly images from the Canon EOS 5D camera were used (4663 images) with a theoretical GSD of  $\approx 0.13$  m. In general, they were not planned for mosaicking and further processing. Using raw images, IMPs were detected, and their locations accurately defined on maps or digital orthophoto maps. The main goal of collecting additional data about SHAs in Gospić, Bilje and Drniš was to prepare evidence so that a proposal could be made to the Croatian Mine Action Centre for starting the process to reduce the SHAs and better assess conditions in the whole considered area. In Gospić, more than five hundred examples of strong IMPs (trenches, bunkers, shelters for heavy weaponry and soldiers) were detected and extracted. Several IMPs were detected in the SHAs in Bilje and Drniš, mainly with lower probability and lower confidence than in the Gospić SHA. Examples of the indicators are shown in Figure 23

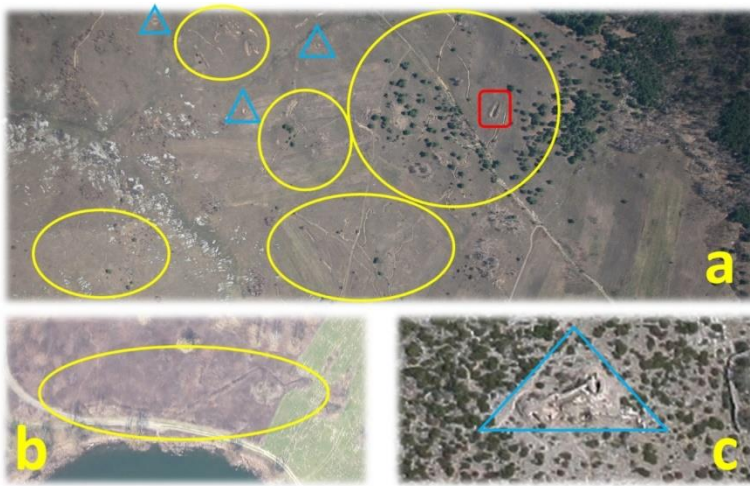


**Figure 23:** Examples of RGB images of parts of the SHAs on which IMPs were noticed in a) Gospić, b) Bilje and c) Drniš gathered at a height of 600 m using a Canon EOS 5D RGB camera. The yellow ellipses mark trenches, the red rectangle a shelter for heavy weaponry, and the blue triangles shelters for soldiers.

### **Imagery of Oil Pollution in the Adriatic Sea and Water Quality in Lake Jarun**

From 12 to 19 October 2008, the National Centre for Coordinating Search and Rescue at Sea (in Croatia) received four alerts from the CleanSeaNet European Maritime Safety Agency (EMSA) about potential oil pollution in the Ecological and Fisheries Protection Zone of the Adriatic Sea. Based on these notifications, flights were carried out using a Mi-8 helicopter on which an AIDSS module for data acquisition was installed for the purpose of finding and documenting the oil pollution. In two cases, oil pollution was confirmed (14 and 16 October 2008) and documented using cameras from the helicopter (through the side doors) and the hyperspectral linear system ImSpector V9 + PixelFly which was located in the sensor pod installed underneath the helicopter. On 14 October, the potential oil pollution was recorded at a height of 300 m and a speed of 33.3 m/s. The average line length was 100 m and the cross-track pixel size was 0.10 m in full spectral range with a

bandwidth of 80 channels and with spectral resolution of 4.4 nm. A raw hyperspectral cube of the sequences was made, consisting of 1,008 hyperspectral linear images. The cube was parametrically referenced as described in the section Production and Parametric Georeferencing of the Hyperspectral Cube (Figure 24b). The RGB image of the oil pollution detected on 14 October 2008 was also referenced (Figure 24a). On the basis of these georeferenced images, classification was carried out along with an estimate of the quantity of spilled oil, according to the Bonn Agreement Oil Appearance Code for visually determining surface density (l/km<sup>2</sup>) [99]. The results of the classification and estimate of the quantity of the oil spill were published and interpreted in [43]. A comparison of the EMSA CleanSeaNet and the airborne assessment of this oil pollution is given in Table 7.

**Table 7:** Data on airborne verification of information on oil pollution provided by EMSA CleanSeaNet service [43].

	EMSA CSN, space-borne SAR sensor	Airborne, hyperspectral and visual sensor
Date	2008-10-14, 07:16 h	2008-10-14, 10:30 h
Coordinates	44° 01' 41" N, 14° 08' 28" E	44° 01' 41" N, 14° 07' 27" E
Area	0.15 sq km	0.015 sq km
Width	0.20 km	0.075 km
Length	0.78 km	0.341 km

A hyperspectral survey of Lake Jarun was carried out on 8 April 2008 at an altitude of 750 m and a speed of 22.2 m/s with a Bell-206 helicopter as the platform. The average line length was 218 m and the line width was 1.63 m. The cross-track pixel size was 0.19 m in full spectral range with a bandwidth of 80 channels and spectral resolution of 4.4 nm. The line of recording was set across the middle of Lake Jarun, running SE-NW. From a sequence consisting of 1,112 hyperspectral linear images, a raw hyperspectral cube was produced which was then parametrically geocoded (Figure 24c and d) using PARGE software. Further processing was carried out on it to analyze the quality of the water in the lake.

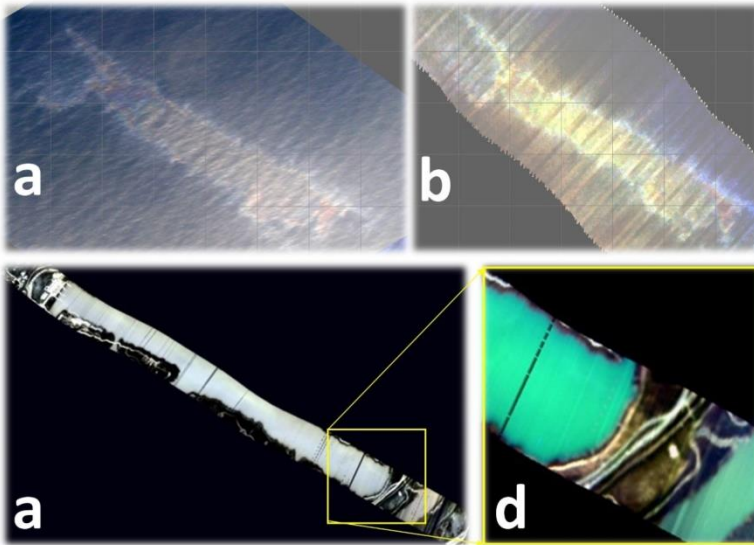


**Figure 24:** a) Georeferenced imagery proving the existence of oil pollution collected by a Sony H2 camera and b) hyperspectral system ImSpector V9 + PixelFly ( $R = 0.755 \mu\text{m}$ ,  $G = 0.645 \mu\text{m}$  and  $B = 0.465 \mu\text{m}$ ). c) Georeferenced hyperspectral cube of Lake Jarun and part of the River Sava and d) enlarged detail of the cube that shows the boundary between the lake and river.

### **Imagery from the Destroyed Munitions Depot in Padjane**

Airborne image collection carried out on 23 April 2015 from a Bell-206 helicopter as a platform covered the whole area of Padjane depot with very high-resolution images in visible wavelengths using a Sony  $\alpha 6000$  camera with a focal length of 35 mm. The flight speed was 20 m/s and the height above the terrain 300m, while the theoretical GSD was 0.03 m. The flight directions for data acquisition were projected according to the lie of the relief, SE-NW and back (meandering), since the wind allowed it. Altogether, 127 images covered the entire area of the destroyed munitions depot, and after triage (blurred images were discarded), 114 images were selected and used to create an orthorectified mosaic image and digital surface model (DSM) (Figure 25). The actual GSD of  $\approx 0.046$  m was determined using a marker for calculating modulation transfer function (MTF), placed on the ground in a position which was secured by soldiers, outside the boundaries of the munitions depot (Figure

25). The primary objective of the aerial survey in the visible spectrum was to provide ground teams with a digital surface model and high-resolution georeferenced orthomosaic of the cleared area, as a visual basis for monitoring clearance actions. The orthomosaic was used by the commander of the clean-up operation to inspect the area, describe the tasks performed, and write a report on the completion of the clearance project.

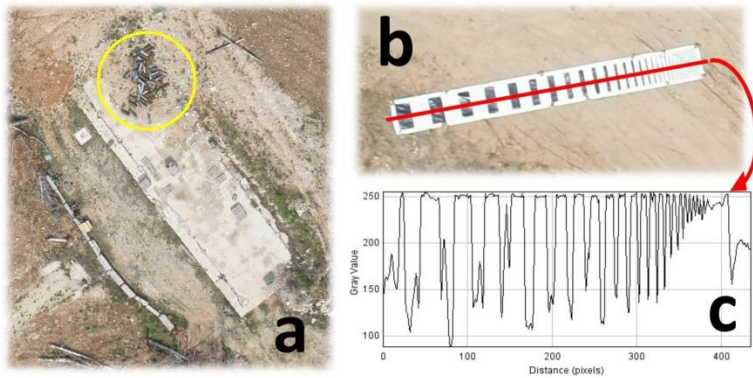


**Figure 25:** Sony a6000 images showing a) a pile of UXOs (yellow circle) and b) marker for calculating modulation transfer function. c) Spectral profile of MTF marker.

### Imagery of Murgiči Site

Murgiči minefield was surveyed on 27 May, and 2 and 3 June 2015. A full-frame hyperspectral camera UHD-185 was mounted on a Bell 206 helicopter and a multirotor remotely piloted X8 MR aircraft. HS cubes were collected from low altitudes to collect high resolution data. The wider region of interest around Murgiči minefield was covered in 6 flights at an altitude of 300 m above mean ground level, while a smaller area was covered by a UAV with 4 routes at 120 m altitude. The mean velocity of the helicopter was around 22 m/s, while for the UAV it was around 4 m/s.

### ImSpector V9 Line Scanner Calibration Procedure Results

A quality assurance procedure performed via MODTRAN reconstructed the atmosphere above for selected targets with

ground-truth measured reflectance. The calculated at-sensor radiance and modelled at-sensor radiance based on in situ measured reflectance are shown in Figure 26a and b. The results obtained demonstrated obvious radiometric/spectral defects, which had to be corrected before undertaking any other action. First, there was full saturation of the brightest targets, which is a typical sign of the poorly calibrated or uncontrolled dynamic range of the system. Second, a highly distorted albedo sequence and lack of gas absorption were clearly demonstrated. Therefore, the spectral/spatial saturation and local spectral stagnation were inspected together with the spectral accuracy of atmospheric gas absorption of the at-sensor radiance data. Figure 26c shows image at-sensor radiance against modelled radiance based on in situ reflectance measuring the reflectance of one selected target. The comparison reveals clear spectral/radiometric differences and distortions. Calculated Rad/Ref and RRDF indices indicated the faulty performance of the sensor, as shown in Figure 27a. In order to avoid saturation of the brightest targets on the image at-sensor radiance, we made an additional RRDF calculation, which did not involve the brightest spectra (radiance and reflectance). Since the sensor was not performing well, the estimation of  $L_{(gain)}$  and  $L_{(offset)}$  was performed by vicarious calibration. Reflectance-based vicarious calibration is used for radiometric recalibration, as image at-sensor radiometric data are calibrated by comparison with the modelled at-sensor radiance based on in situ measured reflectance of selected, well-defined ground targets. During the validation stage, two ground targets were selected and compared. It is important to note that these targets were never included in the recalibration process. They were spectrally measured in situ (reflectance) and stored for the validation stage. The results are presented in Figure 26d and e. At this stage, we can declare that the obtained recalibrated image at-sensor radiance is ready for the next stage - atmospheric correction via calculated coefficients. The final results of the calibration procedure obtained in ENVI are shown in Figure 26f and g.

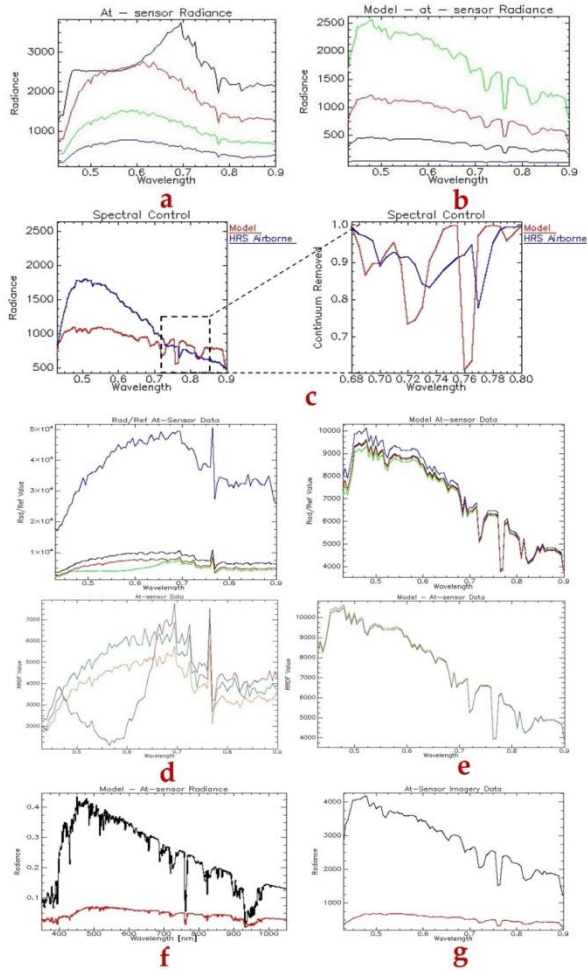


**Figure 26:** a) Image at-sensor radiance and b) modelled at-sensor radiance based on in situ measured reflectance (right side) of four selected ground targets. c) Illustration of radiometric/spectral defects - investigation of image spectral accuracy based on atmospheric gas absorption (blue spectrum) compared with simulated radiance (red) spectrum for the same ground-truth target. d) Image at-sensor Rad/Ref and RRDF, and modelled at-sensor Rad/Ref and e) RRDF based on in situ measured reflectance of four selected ground targets. f) The modelled at-sensor radiance based on in situ measured reflectance and g) image at-sensor radiance.

## Image Mosaics

The mosaicking process is not an integral part of the AIDSS data acquisition module, but the results of the module are the main inputs for mosaicking, so in what follows, examples of manually produced mosaics are given (by determining identical points on the reference and input images) and automatically produced mosaics (using Photoscan software). An example of a manually produced mosaic consisted of 106 VNIR images gathered in 6 series (Figure 27a) from a height of 500 m, using the MS3000 multispectral sensor over of the Vrankovići SHA. The first step was mosaicking along the strip, followed by mosaicking of strips. Mosaicking was done by registering as many identical points as possible on the overlap of two neighbouring images. After mosaicking, the mosaic was geocoded manually by means of the DESCARTES software package with Thin Plate Spline transformation according to 87 common points on the digital orthophoto 1:5000 of the same area (Figure 27a, b and c). The spatial resolution on the digital orthophoto was 0.5 m. The calculated spatial resolution of the VNIR mosaic was 0.15 m. The quality of geocoding was checked at 55 control points in the Vrankovici block mosaic according to the positions of the same points on the reference digital orthophoto image. A manual geocoded image for the same area was created using the LWIR sensor THV with 1000 images collected from a height of 900 m. The RMSE of points on both axes and positions related to the digital orthophoto are given in Table 8.

**Table 8:** Spatial accuracy of manually produced VNIR orthomosaics, measured against check points.

Site (Sensor)	Flight height (m)	GSD (m)	X error (m)	Y error (m)	Total (m)
Vrankovići (MS3100)	500	0.10	± 0.66	± 0.70	± 0.96
Vrankovići (THV 1000)	900	0.53	± 2.19	± 2.16	± 3.08

The mosaic of the destroyed munitions depot in Padjene was created according to StM methodology in Photoscan software, from 114 RGB images taken with a Sony  $\alpha$ 6000 camera. All the

images were upload in PhotoScan and treated as a bundle block with mutual overlapping. Since orientation points were not set up within the depot site, three details were determined which could be recognised on the digital orthophoto depiction before the destruction, and on the mosaic, and the coordinates of these points were entered in Photoscan software as markers, providing a bases for georeferencing the mosaic and DSM of the same area (Figure 27d-f). The coordinates of these three points were read from the 1:5000 digital orthophoto with a spatial resolution of 0.5 m, while the spatial resolution of the aerial photographs was 0.046 m. This led to significant positional and altitudinal errors (Table 7), which were not a problem in this case, because the DSM at the known locations was examined. It was more important to establish whether there were any items of interest (mines or UXO) in the area. A DSM was produced with a point density of 30.6 points per square metre (resolution 0.07 m/pix) and an orthomosaic with a resolution of 0.04 x 0.04 m. The accuracy of absolute positioning in space was not possible to determine for the mosaic of Padjene, since after clearance, it was not possible to find identical points, since the scene looked completely different. The accuracy estimate was therefore only carried out for three points which were used as marked in the Photoscan software (Table 9).

Hyperspectral cubes collected by a UHD 185 full-frame (matrix) camera from the helicopter were used to produce a mosaic of 64,400 m<sup>2</sup> shown in Figure 27g and h. Manual mosaicking was conducted in ENVI SW, based on the identical points of overlapping images. Absolute positioning accuracy for this data set was not calculated, since it was used for a relative comparison of vegetation indices inside and outside the minefield parameter [47].

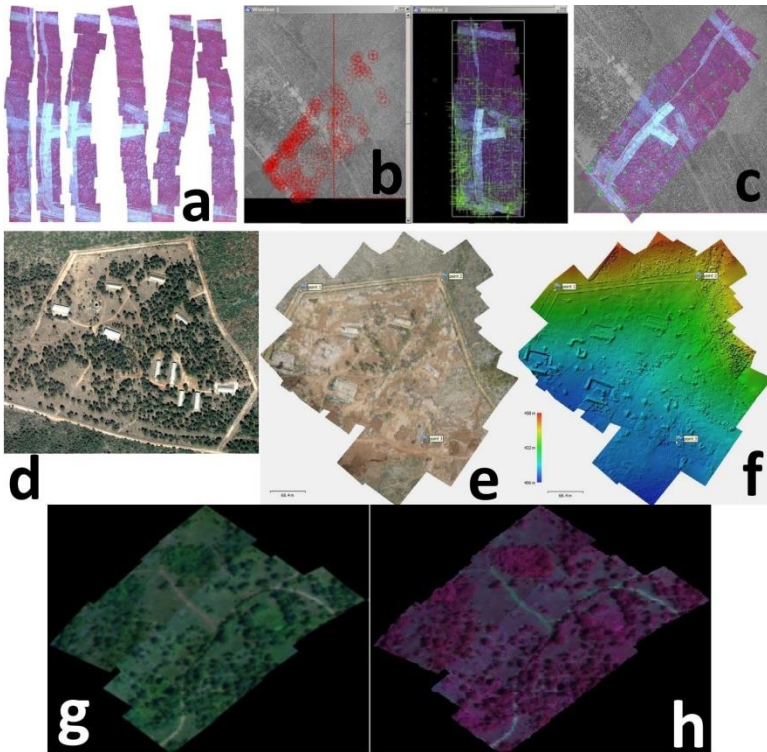


**Figure 27:** a) Strips of VNIR images of the Vrankovići site. b) 87 common points on the mosaic and digital orthophoto 1:5000. c) Geocoded mosaics of the Vrankovići site with 55 control points for accuracy control. d) Digital orthophoto of the munitions depot in Padjane before destruction. e) Orthomosaics of the destroyed munitions depot in Padjane derived from Sony  $\alpha 6000$  images and f) DSM of the same site. g) Mosaic of hyperspectral images for Murgići acquired from the Bell-206 helicopter with full-frame UHD-185camera. Central part of Murgići visualised from a hyperspectral mosaic in RGB (0.65  $\mu\text{m}$ , 0.55  $\mu\text{m}$ , 0.45  $\mu\text{m}$ ) and b) and h) NIR spectral range (0.75  $\mu\text{m}$ , 0.65  $\mu\text{m}$ , 0.55  $\mu\text{m}$ ).

**Table 9:** Spatial accuracy at the control points of the orthomosaic for the Padjene site.

Label	X error (m)	Y error (m)	Z error (m)	Total (m)	Image (pix)
Point 3	-0.80096	-0.82392	-0.06901	1.15115	0.137
Point 1	1.14292	-0.88315	0.41023	1.50150	0.038
Point 2	-0.31536	1.41998	0.22934	1.47254	0.080
Total	0.82608	1.07628	0.27426	1.38420	0.104

## Results of Laboratory and Terrestrial Field Hyperspectral Imaging System

Once all the characteristics, properties and constraints of HSLs V9 and the presented programme codes were defined, the imaging system needed to be characterized and verified to see that it was behaving as described. The focus was on the overall results of the reviewed system introduced in this chapter with all its elements: the hyperspectral imaging system design (HSLs V9), sensor bracket, control system, programme codes for creating the hyperspectral cube, spatial calibration and MTF calculation of the hyperspectral line scanner. In this section, we provide the results of MTF calculation, spatial calibration results in laboratory conditions, and some examples of hyperspectral surveys in the laboratory and in the field, to demonstrate the use of the HSLs V9 as presented. In laboratory conditions, hyperspectral surveying of Roman artefacts found in Sisak, Croatia, was carried out. In addition, as part of terrestrial field work, hyperspectral surveying of vineyards in Jadrtovac (near Šibenik, Croatia) was been carried out. Some of the images are shown in what follows.

### Spatial Calibration Result and Calculation of Modulation Transfer Function

Before the any survey mission, it is necessary to examine the imaging process of the linear scanner in order to perform spatial calibration. Three images of the different camera orientations in relation to the calibration pattern were taken, so that the homologous rays of photogrammetric bundles were intersected as closely as possible to right angles (90 degrees). This ensured

the best geometric conditions for the intersections of the homologous rays, and thus the precise determination of the elements of the inner orientation. The imaging was performed at a distance of 3 m. The results of distortion values of some wavelength, changes of the camera constant (linear scanner) and shifts of the principal point (central pixel) are displayed in Figure 28. The diagrams in Figure 8a-d show the distortion values on the spectral line of the central pixel (zero value) to the margin pixel of the scanner line (450 value in pixels). The diagrams in Figure 28e and f show shifts in the camera constant and principal point of the HSLS V9 system.

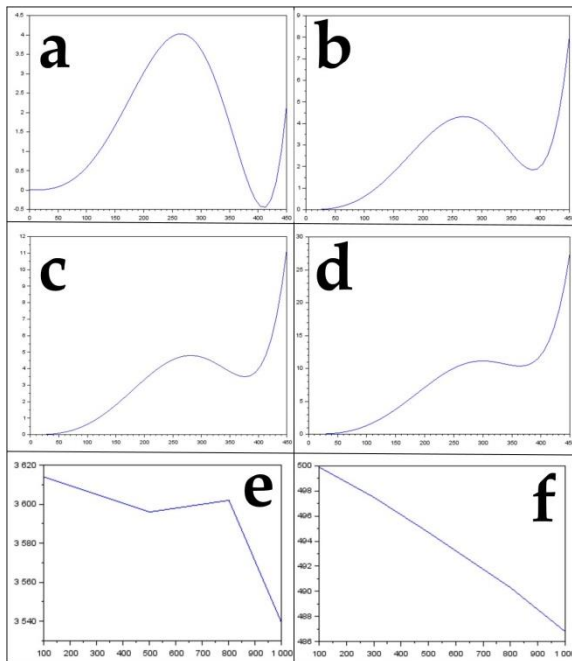


**Figure 28:** Distortion values for the a) blue-indigo (100 pixels from the top of the image), b) yellow-green (300 pixels from the top of the image), c) orange-red (500 pixels from the top of the image, and d) near-infrared (1,000 pixels from the top of the image) parts of the spectrum, while e) shows the camera constant changes in relation to wavelength and f) shows the changes in the position of the principal point in relation to the wavelength. All values on the axis are expressed in pixels.

The value of the distortion curves shows the distortion values within the borders of 0 to 11 for the visible part of the spectrum (Figure 28a, b), while distortion rises drastically at the edges of the image for the near-infrared portion, above 25. This is the consequence of the lack of correction of the lens for chromatic dispersion, for the infrared portion of the spectrum. The analysis of the derived results further shows that as the wavelength changes, the camera constant and position of the principal point also change significantly (Figure 28e and f). The position of the principal point changes almost linearly, within the borders of 499.9 pixels for the blue-indigo portion of the spectrum to 486.8 pixels for the infrared portion, while the camera constant changes from 3.614 pixels for the blue-indigo portion of the spectrum to 3,539 pixels for the near-infrared portion. This change is of a linear character.

Recording of the sample in order to determine MTF for the HSLV V9 was performed at a distance of 1.7 m, with the camera placed so that the slit on the lens of the Inspector V9 was at right angle to the line of the samples. This distance was selected because in laboratory and field conditions, recording is performed at a similar distance, depending on the height of the construction and samples. The result of the recording for the purpose of determining MTF was a 2D image on which the x axis measures the reflectivity of spectral data of the recorded scene for individual wavelengths, and the y axis shows the wavelengths on which the spectral values of each linear sample were recorded (Figure 29a). During recording, the mentioned calibration parameters were used to reduce the distortion effect. Since the spectral component of the adapted HSLV V9 was more important during imaging, the motivation for this research was investigating and detecting changes in the geometric quality linked to certain wavelengths, rather than attempting to determine the geometric quality of the image without errors. MTF was calculated for 10 spectral lines along the entire spectrum from 430 to 900 nm on the image of PixelFly sensor, starting from 0 (the top edge of the image) at intervals of 100 pixels (Figure 29b), in order to establish MTF changes, depending on the wavelengths, under the same conditions, and with the same focus.

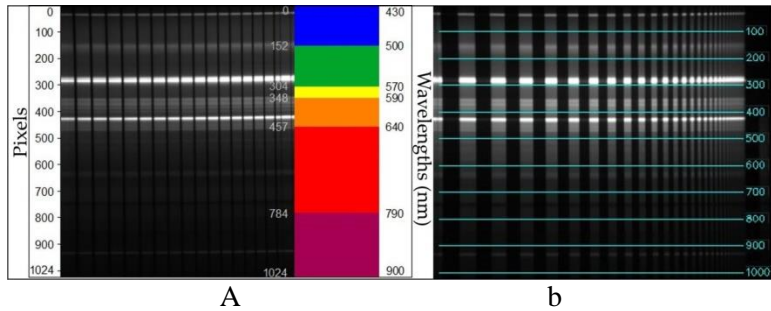


**Figure 29:** a) Distribution of wavelengths in the raw HSLs V9 image, along axis y. b) Positions of the spectral lines for which MTF was calculated (blue transversers lines, while the numbers indicate the ordinal number of the line in relation to the initial line, in pixels).

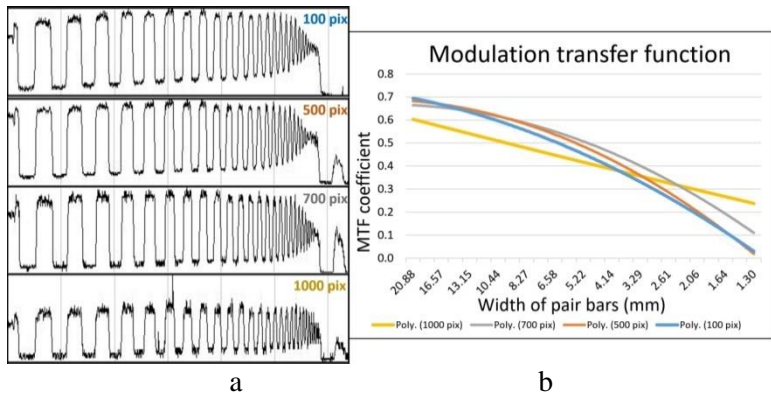


**Figure 30:** a) Spatial frequencies of spectral profile lines for 100, 500, 700 and 1000 pixels. b) Calculated MTFs according to these profiles

Theoretical spatial resolution along the line sensor ( $GSD_v$ ) was 0.48 mm for binning factors 1 ( $(1.7 \text{ m} \times 0.333)/1170$ ), or 0.97 mm for binning factors 2 ( $(1.7 \text{ m} \times 0.333)/585$ ). The values of actual (real)  $GSD_h$  determined on the spectral profile lines were from 100 to 1000 pixels. The values of actual  $GSD_v$  for 4 spectral profiles for 100, 500, 700 and 1000 pixels are listed in Table 10. The derived MTF results (Figure 30) indicate that the sharpness of the images throughout the visible part of the spectrum was equal, and approached Nyquist's theory of digitalization, which should be the result of a specially constructed, high quality lens for hyperspectral measurement (Schneider Kreuznach Xenoplan 1.4/23). This mostly depends

on the resolution of the CCD sensors (in this case, the PixelFly array camera). In fact, the MTF coefficient value fell continuously from the starting value of around 0.7 to 0.1, while the coefficient value in the near-infrared part of the spectrum showed a milder fall. The relationships between theoretical and actual determination along the line sensors ( $GSD_v$ ) is shown in Table 10. An analysis of spatial resolution along the line scanner  $GSD_h$  was not performed.

**Table 10:** Theoretical and actual (determined) spatial resolution along line sensor ( $GSD_v$ ) for the spectral line at 100, 500, 700 and 1000 pixels.

Theoretical $GSD_h$ (mm) (Binning factors 1)	Determined (actual) $GSD_h$			
	100 pixels (mm)	500 pixels (mm)	700 pixels (mm)	1000 pixels (mm)
0.48	0.58	0.58	0.51	0.51

### Laboratory Hyperspectral Surveying of Roman Archaeological Artifacts

We selected fragments of Roman pottery, archaeological artefacts found in the Sisak area in Croatia, as the objects of investigation. Documenting pottery artefacts is one of the main tasks of archaeology, as they were produced in large numbers and have survived in relatively good condition for thousands of years. Archaeologists use pottery to discover information about time periods, trade relations, technological progress, art, politics, religion and many other aspects of ancient cultures. It is rare to discover intact artefacts in archaeological digs. The sites are usually full of fragments which archaeologists can try to rejoin to reconstruct items as far as possible. The main motivation for using the HSLV V9 was to take images of the artefacts for which we know the period when they were created, and to compile a library of spectral responses. The library could be used as a reference to date artefacts about which no information is yet available.

When taking images of the artefacts, dark current imaging was used. It lasted 10 seconds, with a cover over the lens to prevent light from entering. The fragments were scanned using the HSLV

V9 system at a distance of 2 m, with binning factors 1 set and a default gain value of 1. Binning factors 1 were used because we wanted to achieve better spatial resolution along the sensor ( $GSD_v$ ), due to the fact that the objects of interest were small items, archaeological artefacts, or rather, fragments of ancient pottery (Figure 31a). Since the field of view (FOV) of the HSL V9 system is 0.333 % of the distance from object, and the number of effective pixels in the line scanner in binning factors 1 is 1170, the theoretical spatial resolution ( $GSD_v$ ) along the line sensor can be calculated as:

$$GSD_v = \frac{2 \text{ m} \times 0.333}{1170} = 0.00056923 \text{ m} \quad (16)$$

On the other hand, the theoretical spatial resolution across the line sensor ( $GSD_h$ ) can be calculated as:

$$GSD_h = 2 \text{ m} \times 0.00208 = 0.00416 \text{ m} \quad (17)$$

$GSD_h$  or  $GSD_v$  are the sizes which dictates the scanning speed. Since  $GSD_v \approx 4 \text{ mm}$ , the frame rate is 12.5 fps, exposition time is 0.08 s, and scanning speed was calculated according to (14) at 50 mm/s. In this way, we managed to gather continuous spectral lines with no gaps and create a hyperspectral cube with no interpolation between the lines. After imaging, the raw hyperspectral cubes (Figure 31) were produced in the way described in section 3.3. with codes written in the Matlab development environment. The hyperspectral cubes were corrected for the influence of dark current imaging, and atmospheric correction was also performed, since they were created using artificial light at close range.

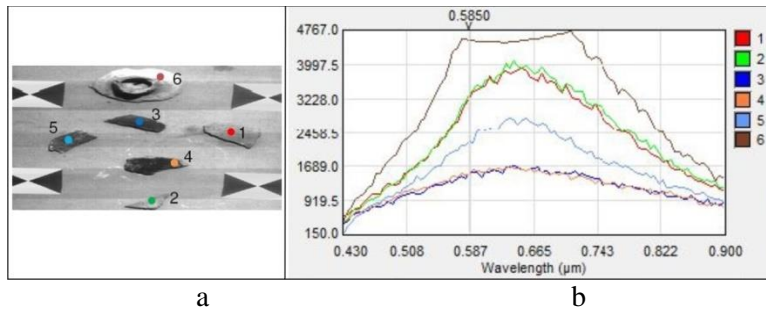


**Figure 31:** a) The hyperspectral view of the archeological artefacts (green band: 0.58  $\mu\text{m}$ , marked 1 to 6) and b) Spectral plot of archeological artefacts from picture a, marked 1 to 6 [94].

## Field Hyperspectral Surveying of Vineyards

In 2014, a trial to simulate various conditions of providing wines with water, consisting of three variants of irrigation and a control variant in which vines were grown without irrigation, was carried out in Jadrtovac, Croatia. The irrigation variations differed in regard to the amount of water provided in relation to the vines' requirements for water. The demands of the plants for water were defined by taking into account the average referential evapotranspiration (ET) (30-year average) from Šibenik meteorological station, precipitation at the trial plantation, and the features of the vines in the area. The variants and trial labels were:

- Variant A: 50% ET – irrigation providing 50% of the calculated requirements of the vines for water (delivered by a single pipe with a diameter of 1 cm)
- Variant B: 75% ET – irrigation providing 75% of the calculated requirements of the vines for water (delivered by two pipes with diameters of 1 cm)
- Variant C: 100% ET - irrigation providing 100% of the calculated requirements of the vines for water (delivered by three pipes with diameters of 1 cm)
- Control variant: no irrigation.

The hyperspectral pilot surveying of the plantation in the named location was carried out on 30 July 2015. All four rows were

surveyed (the control and three irrigation variants) in two sections, each 2.4 m long. In this case too, dark current imaging was used, as with the artefacts. The HSLS V9 was used with binning factors 2 and a default value of gain of 1, from 12:30 to 14:45 hours, from a metal construction fixed to a trailer pulled from site to site by a tractor (Figure 32a). The actual surveying was performed when the construction was at rest and its engine was operating the HSLS V9. The stony surfaces between the rows were covered in dark plastic netting in order to reduce the effect of light from the surroundings. Binning factors 2 were used because the area between the rows of vines was homogeneous and the data on spectral response from the area for further processing were more important, in other words, calculating 16 different types of vegetation indices.

For the same reason, parametric georeferencing of the hyperspectral cubes was not performed. The system was placed approximately 3.7 m above the ground, while the tops of the vines were about 1.2 m from the ground. Thus, the tops of the vines (top leaves) were about 2.5 m from the lens. Accordingly, the theoretical spatial resolution ( $GSD_v$ ) along the line sensor with binning factors 2 were 1.4 mm, and the theoretical spatial resolution ( $GSD_h$ ) across the line sensor was 5.2 mm.  $GSD_v \approx 1.4$  mm, the frame rate was 24 fps, the exposition time was 0.042 s, and the speed of the HSLS V9 was calculated according to (7) at 33 mm/s. Raw hyperspectral cubes were created from the spectral lines, as described in section 2.3 (without parametric georeferencing) for each surveyed part of each row surveyed, than all four cubes were merged in a mosaic showing all four rows next to each other (Figure 32b). Quick atmospheric correction in the ENVI programme package was carried out on the mosaics of all four hyperspectral cubes.

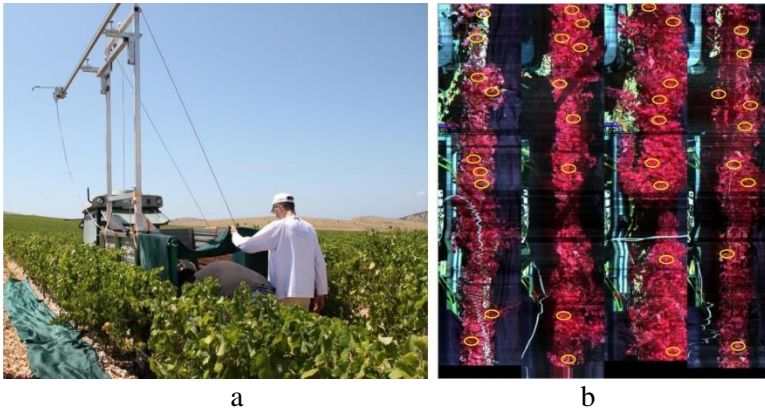


**Figure 12:** a) Sensor bracket, HSLs V9 and control system during hyperspectral survey in Jadrtovac vineyard. b) Mosaic of four hyperspectral cubes (with a combination of wavelengths: 850, 650, 550 nm) with places marked where samples were taken to calculate vegetation indices.

After processing the hyperspectral cubes, the ENVI programme package was used to calculate 16 selected vegetation indices, which served agronomists as input data for the complex analysis of chlorophyll and moisture in the vines [54]. The authors of this paper did not participate in this analysis, and it does not form an integral part of our article, but the calculated values of 5 vegetation indices are given (Figure 33.) to illustrate the potential of the HSLs V9 in similar situations.

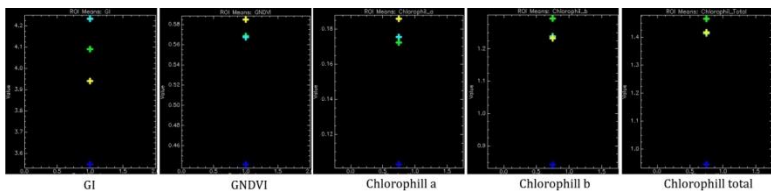


**Figure 33:** Medium value diagrams for vegetation indices: Greenness index (GI), Green normalised difference vegetation index (GNDVI), Chlorophyll a, Chlorophyll b and Total chlorophyll. Legend: blue – variant A, light blue – variant B, yellow – control row, green – variant A, light blue – variant B, yellow – control row.

## Discussion and Conclusion

The results (Table 11) showed that the helicopters tested were the right choice for surveying larger regions of interest with

coarser spatial resolution data requirements. In comparison with RPASs, helicopters have higher payload limits and endurance, but velocity and altitude values are much higher, as are vibrations. When choosing between the smaller helicopters (Bell-206, Gazela) and the larger Mi-8, the following should be taken into account: smaller helicopters have lower altitudes, velocity, and vibrations, but have payload limitations – they can carry a multispectral survey system and only one system operator. In addition, validation tests of the helicopters show that controlling the platform when executing planned survey routes can be a challenge, since correction of the yaw (direction angle) dramatically enlarges the values of the roll and pitch parameters (swinging).

The results of the operational testing performed for two RPASs (Table 11) showed that these particular models struggled to maintain stability due to borderline payload, which caused deviation from planned routes. Payload limitation also dramatically affected the endurance of the system, restricting operational deployment. On the other hand, these platforms performed at low altitudes and velocities with low vibration, and showed a satisfactory reduction in the value of pitch and roll parameters. For the operational deployment of the T-LHSIS system, heavy lift RPAS should be used. The blimp was rejected as a suitable platform due to several drawbacks: (I) sudden, large changes of roll and pitch values during flight caused major distortions of hyperspectral images, (II) it required relatively high velocity and altitude values to obtain stable platform flight regime, (III) there was low controllability during flight.

**Table 11:** Summarized results of tests performed in different operational conditions for the following platforms: Mi-8 and Bell-206 helicopters, UAV X8 MR, UAV 8 ZERO, and a blimp with hyperspectral line scanner V9, multirotor UAV with hyperspectral frame sensor UHD-185.

Platform	Min. Velocity (m/s)	Swinging	Payload ( $\approx$ 4 kg)	Vibration	Controllability
Mi-8 helicopter	33	Relatively stable	High	High	Good
Bel-206 helicopter	20	Relatively stable	Relatively high	Medium	Good
UAV X8 MR (smaller)	1 - 4	Medium - roll span: 2.8° - 4.5°, - pitch span: 1.2° - 2.0°)	Borderline	Low	Executed routes significantly deviated from the planned ones
UAV 8 ZERO (smaller)	4 - 5	Medium - roll span: 3.3° - 5.6°, - pitch span: 1.2° - 2.0°)	Sufficient	Low	Executed routes significantly deviated from the planned ones
Blimp	4 - 5	Very high - roll span > 20°, - pitch span > 10°)	Sufficient	Low	Difficult to navigate during flight (large yaw)

The primary goal of the AIDSS module for gathering aerial data in crisis situation was to acquire high quality inputs for further processing according to the AIDSS methodology. From the above, it is clear that this was achieved by selecting platforms and sensors for specific missions. For an initial insight into the scene, imaging from a height of 600 m was conducted (or higher, depending on the size of the area and the need to process information as quickly as possible). Next, RPAS was used to record individual parts of scenes of particular importance, with sufficient GSD to identify the indicators in them. All the images of the visible sensors had sufficient GSD to detect the target AIDSS indicators (IMP, oil pollution, vegetation cover, surface waters, UXOs, etc.). Other sensors were used to supplement the view of situation (potential elimination of dubious elements when drawing conclusions) and for specific purposes; in the case of the hyperspectral sensor, to discern vegetation inside and outside the minefields.

Within the framework of the research conducted in six international and domestic scientific projects, an AIDSS module for aerial data acquisition in crisis situations and environmental protection was developed, tested and implemented in operational (real) conditions. This system was developed primarily for aerial non-technical surveys in humanitarian mine action, where it was implemented most and had significant achievements in detecting IMPs and assisting demining experts in SHA reduction. Its main component is a multi-sensor system that provides imagery from the visible, infrared and thermal infrared part of the very high resolution spectrum for the photointerpretation and extraction of indicators. Low-cost visible digital cameras provide GSD from 1 to 11 cm for flight heights from 50 to 1000 m, multispectral and hyperspectral sensors from 2 to 28 cm, and thermal infrared sensors from 3 to 60 cm. The benefit of using this multisensory system imagery was demonstrated in a number of case studies in which IMPs were detected and extracted, and the existence of oil pollution in the Adriatic Sea was detected and extracted by producing orthomosaics (from RGB and hyperspectral images) for further research. In spite of the fact that the module was not conceived as a system for strict photogrammetric recording of inaccessible terrains, it provides the potential for georeferencing

images and creating orthomosaics. The system is customizable for different types of platforms, for which special pods are constructed with different sensor and electricity power supply configurations. In the research, mostly off-the-shelf equipment and software were used, but some software solutions for the image collection of hyperspectral data and production of raw and parametrical georeferenced hyperspectral cubes were made specially and are presented in this paper. One type of software developed and described in the research is the recorder for controlling and management (selecting various parameters for the best adjustment to atmospheric conditions) during recording by multispectral, thermal and hyperspectral module sensors. The development of the system began using helicopters as platforms and continued using RPAS, as they developed and increased their flight and load-bearing characteristics. The module was developed to be as independent as possible of the platform used, with the potential to adjust and use it on various airborne platforms, with minimal modifications. Another condition for the use of this module is the potential to map the indicator on the image (the indicator must be visible in the picture), so it is most important to define an acceptable list of indicators for a phenomenon at the scene.

Of course, there are limitations when using this module. The main limitation is aerial data acquisition over forested regions, where it is impossible to see beneath the foliage and set ground control points on the terrain for the purpose of more accurate georeferencing of images and mosaics, and indicators detected on them. However, the use of programme tools such as UgCS Mission Planning Software (<https://www.ugcs.com/>) within the AIDSS data acquisition module may reduce such limitations and enhance the value of the entire system, which was used in a non-technical survey conducted by T-AIDSS's Module for Data Acquisition on SHA after the impact of landslides, floods and torrent on them in Bosnia and Herzegovina in 2016.

The HSL5 V9 line scanner based hyperspectral imaging system described in this chapter shows promise for agricultural (grapevine) applications. It may be a useful remote sensing tool for hyperspectral remote sensing methods in laboratory and

terrestrial applications. The horizontal and vertical binning capability of the line scanner allows images with various spatial and spectral resolutions along the line scanner (GSD<sub>v</sub>) to be created. The intention behind the use of the HSLs V9 is to survey a scene or samples from a construction at a distance of about 3 m, and the emphasis is on the spectral and spatial characteristics of the recorded objects.

The most common approach to calibrating the line sensor in close-range applications is to derive the calibration model using one 3-D-pattern image specifically constructed for the particular application [63]. Another concept is to extend one-dimensional imaging by one more spatial dimension [64]. The mathematical model used in this research of linear array sensor imaging is transformed to the mathematical model (with one line and many columns), for which many calibration algorithms have already been developed. Thus, the mathematical model of the spatial calibration of the line scanner differs from the mathematical model applied in spatial photogrammetric reconstruction. In this model, the mathematical model of calibration corresponds to the mathematical model of spatial reconstruction. This enables the impact of calibration results on the quality of spatial reconstruction to be tracked and analyzed. So, using the parameters of inner orientation obtained by the proposed calibration method in the geocoding of hyperspectral cubes, a significant increase in the positional accuracy of every geocoded pixel in the hyperspectral cube can be achieved. In fact, this means producing a mathematical imaging model aligned with the ideal central projection of the area in a 1-D sensor model, extended to account for the distortion influence using the Brown distortion model with seventh-degree polynomial correction.

Compared to the usual calibration model of industrial line scanners, it should be noted that this model is adapted to industrial applications, where quick, automatized calibration on a pre-defined sample must be carried out, and during which the laws of central projection of a line from the area to a line on the image and determination of equations of collinearity are used for the mathematical model. This avoids the limiting requirement (for conducting photogrammetric calibration) that the sample

must be in a single plane. This model is used to determine the effect of radial distortion.

The results of the research show that the inner calibration parameters depend significantly on the wavelength of the light falling on the sensor. Similarly, the degree of this influence depends crucially on the quality of the lenses used in the multispectral or hyperspectral cameras. The use of lenses that are carefully corrected for chromatic dispersion (achromatic, or better still, apochromatic) is recommended, as they reduce the effect of light wavelengths on calibration elements to some extent, although they do not rule it out entirely. In this, the trend of change in the position of the main point is almost completely linear, ranging from 499.9 px for the blue-indigo part to 486.8 px for the infrared part of the spectrum, with a mean determination error of around 0.1 px. The focal distance also changes from 3614 px (blue-indigo channel) to 3539 (near infra-red channel), and the change is non-linear. These results clearly show that the light wavelength used when calibrating the hyperspectral scanner must be taken into account.

For high-quality modelling of the calibration parameters, calibration must be performed for the border and median wavelengths of the spectrum within which imaging is to be carried out. In exceptional cases, calibration can be performed using the middle part of the spectrum. The effect of distortion is not negligible either, and ranges from 4 px for the blue-indigo to 25 px for the near infra-red part of the spectrum (on the line edges), where the distortion effect increases sharply. Therefore, when calibration is performed, it is absolutely necessary to account for distortion parameters and use them to eliminate systematic distortion in the imaging results.

An assessment of the quality of HSL optical imaging, using the modulation transfer function, has shown that the sharpness of the imaging throughout the entire visible part of the spectrum is the same and approaches Nyquist's digitalization theory. This is the consequence of a specially constructed, high-quality lens for hyperspectral surveying, and depends mainly on the resolution of the CCD Pixelfly sensor. In fact, the coefficient of the

modulation transfer function falls almost linearly from an initial value of 0.7 to 0.1, with a borderline frequency of around 0.3 cy/px for blue, and to 0.6 cy/px for near infrared. It is interesting to note that the borderline frequency for the near-infrared area is almost twice as high in relation to the visible part of the spectrum.

The results presented in this chapter in the form of hyperspectral cubes are useful in a spectral analysis of archaeological artefacts and the vines in the Jadrtovac area. The differences in the values of the calculated vegetation indices provides agronomic experts with high-quality input data for a decision support system to manage vines and vine products. Some archaeological artefacts have quite different spectral responses (signatures) in the portion of the spectrum between 0.580 and 0.740  $\mu\text{m}$ . In this area, there is the potential to distinguish between artefacts 5 and 6, while pairs 1 and 2, and 3 and 4 have very similar common spectral responses, while differing considerable from pair 5 and 6. In the second case, difference in the values of selected vegetation indices were obvious, giving agronomic experts good quality input data for a decision support system to manage vines and vine products.

## References

1. Human Rights Watch. Landmine Monitor Report 1999: Toward a Mine-Free World. International Campaign to Ban Landmines. USA. 1999.
2. IMAS 04.10. Glossary of mine action terms, definitions and abbreviations, Second edn. 2014. Available online at: <https://www.mineactionstandards.org/fileadmin/MAS/documents/imas-international-standards/english/series-04/IMAS-04-10-Ed2-Am3.pdf>
3. Maathuis BHP. Remote Sensing Based Detection of Minefields. Geocarto International. 2003; 18: 51-60.
4. IMAS 08.10. General mine action assessment, Second edn. 2003. Available online at: <https://www.mineactionstandards.org/fileadmin/MAS/documents/imas-international-standards/english/series-08/IMAS-08-10-Ed2-Am1.pdf>

5. IMAS 04.20, Technical Survey, Second edn. 2010. Available online at: [https://www.mineactionstandards.org/fileadmin/MAS/documents/nmas-national-standards/sri-lanka/SLNMAS\\_04-20\\_-\\_Technical\\_Survey.pdf](https://www.mineactionstandards.org/fileadmin/MAS/documents/nmas-national-standards/sri-lanka/SLNMAS_04-20_-_Technical_Survey.pdf)
6. Bajić M, Matic C, Krtalic A, Candjar Z, Vuletic D. Research of the mine suspected area. HCR Centre for testing, development and training Ltd. Zagreb: Sortina 1 d, 10000 Zagreb, Croatia, 2011. Available online at: <https://www.ctro.hr/hr/publikacije>
7. Matić Č, Laura D, Turšić R, Krtalić A. Analytical assessment for the process of collecting additional data on a suspected hazardous area in humanitarian demining. Publication, CROMAC-CTDT Ltd. Zagreb. 2014, Available online at: <http://www.fp7-tiramisu.eu/sites/fp7-tiramisu.eu/files/publications/Analytical%20assessment%20of%20the%20process%20of%20collecting%20additional%20data%20on%20a%20suspected%20hazardous%20area%20in%20humanitarian%20demining.pdf>
8. van Genderen J, Maathuis B. Pilot Project for Airborne Mine-field Detection in Mozambique (Angola project). EC-DG8, UK, Netherlands, Luxembourg, Sweden, United Kingdom, Portugal, Belgium, Germany, Norway. 1999.
9. Maathuis B. Remote Sensing Based Detection of Landmine Suspect Areas and Minefields. Dissertation. International Institute for Aerospace Survey and Earth Sciences. Enschede, The Netherlands. 2001.
10. Yvinec Y, Milisavljevic N, Beumier C, Mahamadou I, Borghys D, et al. Chapter 5 - Remote Sensing for Non-Technical Survey. In Mine Action - The Research Experience of the Royal Military Academy of Belgium. London: INTECH. 2017; 634-726.
11. Maathuis BHP, van Genderen JL. A review of satellite and airborne sensors for remote sensing based detection of minefields and landmines. International Journal of Remote Sensing. 2004; 25: 5201-5245.
12. Yvinec Y. A validated method to help area reduction in mine action with remote sensing data. In: Lončarić S, Babić H, Bellanger M, editors. Proceedings of 4th International

- Symposium on Image and Signal Processing and Analysis (ISPA 2005). Zagreb, Croatia. 2005; 6.
13. Bajić M. The Advanced Intelligence Decision Support System for the Assessment of Mine-suspected Areas. *The Journal of ERW and Mine Action*. 2010; 69-75.
  14. Krtalić A, Bajić M. Development of the TIRAMISU Advanced Intelligence Decision Support System, *European Journal of Remote Sensing*. 2019; 52: 40-55.
  15. Eisl M, Khalili M. ARC – Airborne Minefield Area Reduction, In *Proceedings of the International Conference Requirements and Technologies for the Detection, Removal and Neutralization of Landmines and UXO*. Brussels, Belgium. 2003; 7.
  16. Fiedler T, Bajić M, Gajski D, Gold H, Pavković N, et al. System for Multi-sensor Airborne Reconnaissance and Surveillance in Crisis Situations and Environmental Protection (Final report of Technology project TP-006/0007-01 (Internal document in Croatian for GF, CTRO, FTTS). Zagreb, Croatia. Faculty of Geodesy University of Zagreb. 2008.
  17. Bajić M, Krtalić A, Gold H, Čandjar Z, Vuletić D, et al. Deployment of the Decision Support System for Mine Suspected Area Reduction, Final Report (Final Report 2009, V1.0.0 - Internal document for ITF, CTRO, BH MAC), Zagreb, Croatia: CROMAC Center for Testing, Development and Training, Ltd. & Ig, Slovenia: International Trust Fund for Demining and Mine Victims Assistance. 2009a.
  18. Bajić M, Krtalić A. Deployment of the Advanced Intelligence Decision Support System for Mine Suspected Area Reduction in Bosnia and Herzegovina (Final report 2009, V2.0.0 – Internal document for ITF, CTRO). Zagreb, Croatia: CROMAC Centre for Testing, Development and Training, Ltd., Ig, Slovenia: International Trust Fund for Demining and Mine Victims Assistance & Sarajevo, Bosnia and Herzegovina: MAC of Bosnia and Herzegovina. 2009b.
  19. Yvinec Y, Baudoin Y, De Cubber G, Armada M, Marques L, et al. TIRAMISU: FP7-Project for an integrated toolbox in Humanitarian Demining, focus on UGV, UAV and technical survey. In *Proceedings of 6th IARP Workshop on Risky*

- Interventions and Environmental Surveillance (RISE). Warsaw, Poland. 2012; 17.
20. IMAS 08.10. Non-technical survey, First edn. 2009. Available online at: <https://www.mineactionstandards.org/fileadmin/MAS/documents/imas-international-standards/english/series-08/IMAS-08.10-Ed.1-Am2.pdf>
  21. Bajić M, Ivelja T, Hadžić E, Balta H, Skelac G, et al. Impact of Flooding on Mine Action in Bosnia and Herzegovina, Croatia, and Serbia. Journal of ERW and Mine Action. 2015; 43-49.
  22. Mostafa MRM, Swarz KP. A Multi-Sensor System for Airborne Image Capture and Georeferencing. *Photogrammetric Engineering & Remote Sensing*. 2000; 66: 1417-1423.
  23. Wang J. An airborne multi- angle TIR/VNIR imaging system, *Remote Sensing Reviews*. 2000; 19: 161-169.
  24. Akihisa W, Toshiaki Y, Masaaki M, Takanari, A., Hideo, A. & Hirokazu, T. A Surveillance System Using Small Unmanned Aerial Vehicle (UAV) Related Technologies, *NEC Technical Journal. Special Issue on Solving Social Issues through Business Activities*. 2013; 8: 68-73.
  25. Turner D, Lucieer A, Malenovský Z, King D, Robinson S. Spatial Co-Registration of Ultra-High Resolution Visible, Multispectral and Thermal Images Acquired with a Micro-UAV over Antarctic Moss Beds. *Remote Sensing*. 2014; 6: 4003–4024.
  26. Simeone A, Watson N, Sterritt I, Woolley E. A Multi-sensor Approach for Fouling Level Assessment in Clean-in-place Processes. *Procedia CIRP*. 2016; 55: 134–139.
  27. Varshney PK. Multisensor data fusion. *Electronics & Communication Engineering Journal*. 1997; 9: 245–253.
  28. Khaleghi B, Khamis A, Karray FO, Razavi SN. Multisensor data fusion: A review of the state-of-the-art. *Information Fusion*. 2013; 14: 28–44.
  29. Bloch I, Milisavljević N, Acheroy M. Multisensor Data Fusion for Spaceborne and Airborne Reduction of Mine Suspected Areas. *International Journal of Advanced Robotic Systems*. 2007; 4: 173-186.

30. E Waltz, J Llinas. *Multisensor Data Fusion*. Norwood: Artech House, Inc. ©1990.
31. Liggins ME, Hall DL, Llinas J. *Handbook of multisensor data fusion: theory and practice*, 2nd ed. Boca Raton: CRC Press, Taylor & Francis Group. 2008.
32. Hackett MK, Mubarak S. Multi-sensor fusion: a perspective. In *Proceedings of the IEEE International Conference on Robotics and Automation*. Cincinnati, USA. IEEE. 1990; 1324–1330.
33. Habib MK. Humanitarian demining: Mine detection and sensors, In *Proceedings of the IEEE International Symposium on Industrial Electronics*. Gdansk, Poland. IEEE. 2011; 2237–2242.
34. Lou CR, Chang CC, Lai CC. Multisensor Fusion and Integration: Theories, Applications, and its Perspectives, *IEEE Sensors Journal*. 2011; 11: 3122-3138.
35. Rao BSY, Durrant-Whyte HF, Sheen JA. A Fully Decentralized Multi-Sensor System For Tracking and Surveillance. *The International Journal of Robotics Research*. 1993; 12: 20–44.
36. Robledo L, Carrasco M, Mery D. A survey of land mine detection technology. *International Journal of Remote Sensing*. 2009; 30: 2399–2410.
37. Habib MK. Humanitarian demining: Reality and the challenge of technology – The state of the arts. *International Journal of Advanced Robotic Systems*. 2007; 4: 151–172.
38. Santana P, Barata J. Unmanned helicopters applied to humanitarian demining, In *Proceedings of 10th IEEE Conference on Emerging Technologies and Factory Automation (ETFA 2005)*. Catania, Italy. 2005; 1: 729-738.
39. Castiblanco C, Rodriguez J, Mondragon I, Parra C, Colorado J. Air Drones for Explosive Landmines Detection, in book *ROBOT2013: First Iberian Robotics Conference*. Advances in Intelligent Systems and Computing. In: Armada M, Sanfelin A, Ferre M, editors. *Advances in Robotics*. Switzerland: Springer International Publishing. 2014; 2: 107–114.
40. Nikulin A, de Smet T, Baur J, Frazer W, Abramowitz J. Detection and Identification of Remnant PFM-1 “Butterfly

- Mines” with a UAV-Based Thermal-Imaging Protocol. Remote Sensing. 2018; 10: 1672.
41. Fardoulis JS, Smith DA, Payton OD, Scott TB, Freer JE, et al. Deploying Low Cost, Small Unmanned Aerial Systems in Humanitarian Mine Action. In: Brkljačić A, editor. Proceedings of The 14th International Symposium MINE ACTION 2017. Biograd, Croatia. Zagreb, Croatia, HCR-CTRO. 2017; 111-118. Available online at: <https://www.ctro.hr/en/publications/category/34-simpozij-protuminsko-djelovanje-book-of-papers>
  42. SenseFly. Enhancing Mine Action Operations with High-Resolution UAS Imagery, Case study. 2016. Available online at: [https://www.gichd.org/resources/publications/detail/publication/enhancing-mine-action-operations-with-high-resolution-uas-imagery/#.XHj8-KAo\\_5c](https://www.gichd.org/resources/publications/detail/publication/enhancing-mine-action-operations-with-high-resolution-uas-imagery/#.XHj8-KAo_5c)
  43. Bajić M. Airborne Hyperspectral Surveillance of the Ship-based Oil Pollution in Croatian Part of the Adriatic Sea. Geodetski list. 2012; 2: 77-100.
  44. Eisl M, Khalili M. ARC – Airborne Minefield Area Reduction, In Proceedings of the International Conference Requirements and Technologies for the Detection. In: Sahli H, Bottoms AM, Cornelis J, editors. Removal and Neutralization of Landmines and UXO. Brussels, Belgium. VUB-ETRO, Brussels, Belgium. 2003; 7.
  45. Bajic M, Gold H, Pračić Ž, Vuletić D. Airborne sampling of the reflectivity by the hyperspectral line scanner in a visible and near infrared wavelengths. In: Marinko O, editor. Proceedings of the 24th Symposium of the European Association of Remote Sensing Laboratories. Dubrovnik, Croatia. Rotterdam: Millpress. 2004; 703-710.
  46. Šemanjski S, Gajski D, Bajić M. Transformation of the Hyperspectral Line Scanner into a Strip Imaging System. In: Olučić, Marinko, editors. Proceedings of Symposium of the European Association of Remote Sensing Laboratories. New Strategies for European Remote Sensing. Dubrovnik, Croatia. Rotterdam: Millpress. 2005; 369-376.
  47. Bajic M, Ivelja T, Brook A. Developing a Hyperspectral Non-Technical Survey for Minefields via UAV and

- Helicopter, *Journal of Conventional Weapons Destruction*. 2017; 21: 1, Article 11.
48. Behmann J, Mahlein A, Paulus S, Kuhlmann H, Oerke E, et al. Calibration of hyperspectral close-range pushbroom cameras for plant phenotyping, *ISPRS Journal of Photogrammetry and Remote Sensing*. 2015; 106: 172–182.
  49. Miljković V. Spatial Calibration of Multispectral and Hyperspectral Sensors in Close-Range Photogrammetry, PhD Thesis. Faculty of Geodesy. University of Zagreb. Zagreb (in Croatian). 2017.
  50. Miljković V, Gajski D, Vela E. Spatial Calibration of the Hyperspectral Line Scanner by the Bundle Block Adjusting Method. *Geodetski list*. 2017; 2: 127–142.
  51. Boreman GD. Modulation transfer function in optical and electro-optical systems. WA: SPIE press. 2001; 21.
  52. Rossmann K. Point Spread-Function, Line Spread-Function, and Modulation Transfer Function. *Radiology*. 1969; 93: 257–272.
  53. Petković D, Shamshirband S, Saboohi H, Ang TF, Anuar NB, et al. Evaluation of modulation transfer function of optical lens system by support vector regression methodologies. A comparative study, *Infrared Physics & Technology*. 2014; 65: 94–102.
  54. Alaruri SD. Calculating the modulation transfer function of an optical imaging system incorporating a digital camera from slanted-edge images captured under variable illumination levels: Fourier transforms application using MATLAB, *Optik-International Journal for Light and Electron Optics*. 2016; 127: 5820–5824.
  55. Achery M, Yvinec Y. Chapter 3: Mine-suspected Area Reduction Using Aerial and Satellite Images. In: Maki K Habib, editors. *Book Humanitarian Demining: Innovative Solutions and the Challenges of Technology I-Tech Vienna: Education and Publishing*. 2008; 69-94.
  56. SMART. Space and airborne mined area reduction tools – SMART, EC IST–2000-25044. 2000. Available online at: <http://www.smart.rma.ac.be>
  57. MZOS RH project: System for Multi-sensor Airborne Reconnaissance and Surveillance in Crisis Situations and Environmental Protection TP-06/0007-01, funded by

- Ministry of Science and Education of the Republic of Croatia. Zagreb, Croatia. 2007.
58. Acheroy M. Mine action: status of sensor technology for close-in and remote detection of anti-personnel mines. *Near Surface Geophysics*. 2006; 5: 43–55.
  59. Nuzzo L, Alli G, Guidi R, Cortesi N, Sarri A, et al. A new densely-sampled Ground Penetrating Radar array for landmine detection. *Proceedings of the 15th International Conference on Ground Penetrating Radar*. Brussels, Belgium. 2014; 969-947.
  60. Baudoin Y. TIRAMISU: Technical survey, close-in-detection and disposal mine actions in Humanitarian Demining: challenges for Robotics Systems. 2013. Available online: <http://www.fp7-tiramisu.eu/sites/fp7-tiramisu.eu/files/publications/KN%20Clawar%20Baudoin.pdf>
  61. Šipoš D, Gleich D, Malajner M. Stepped Frequency and Pulse based radars for landmine detection. In the *Proceedings of 16<sup>th</sup> International Symposium Mine Action*. 2019, 8 - 11 April. Slano, Croatia. 2019; 16-20.
  62. TIRAMISU. (2012-2015): Toolbox implementation for removal of antipersonnel mines, submunitions and UXO (European Community's Seventh Framework Programme (FP7/2007-2013). Collaborative Project – Large-scale Integration Project, FP7-SEC-2011-1, Grant Agreement Number 284747, FP7-SEC 2011-284747). Available online at: <http://www.fp7-tiramisu.eu/>
  63. ARC. Airborne Minefield Area Reduction – ARC, EC IST-2000-25300. 2000. Available online at: <https://cordis.europa.eu/project/rcn/54367/factsheet/es>
  64. ITF Deployment of the Decision Support System for Mine Suspected Area Reduction. International Trust Fund for Demining and Mine Victims Assistance, Ig, Slovenia and HCR Center for Testing. Zagreb: Development and Training, Ltd. 2008-2009.
  65. Lacroixa V, Vanhuyse S. Indicators of mine presence: Focus on trenches, *South Eastern European Journal of Earth Observation and Geomatics*. 2014; 3: 653-639.
  66. Vanhuyse S, Hanson E, Wolff E, Hölbling D, Friedl B, et al. Object-based Image Analysis for Detecting Indicators of

- Mine Presence/Absence to Support Suspected Hazardous Area Re-delineation in the Republic of Croatia, South Eastern European Journal of Earth Observation and Geomatics. 2014; 3: 525-529.
67. Katartzis A, Vanhamel I, Chan JCW, Sahli H. Remote sensing minefield area reduction: semantic knowledge-based image understanding. In: H Lacoste, L Ouwehand, editors. Proceedings of the ESA-EUSC 2004 - Theory and Applications of Knowledge-Driven Image Information Mining with Focus on Earth Observation (ESA SP-553). Published on CDROM. Madrid, Spain. 2004; 19.
  68. Katartzis A, Sahli H, Pizurica V, Cornelis J. A model-based approach to the automatic extraction of linear features from airborne images. IEEE Transactions on Geoscience and Remote Sensing. 2001; 39: 2073–2079.
  69. van Kempen L, Katartzis A, Pizurica V, Cornelis J, Sahli H. Digital signal/image processing for mine detection. Part1: Airborne approach, Proc. of MINE'99. Euroconference on Sensor systems and signal processing techniques applied to the detection of mines and unexploded ordnance, 1-3 October. Firenze, Italy. 1999; 48-53.
  70. McFee JE, Achal S, Ivanco T, Anger C. A short wave infrared hyperspectral imager for landmine detection, In Proceedings of the Detection and Remediation Technologies for Mines and Minelike Targets X. Orlando, Florida, US. 2005.
  71. Makki I, Younes R, Francis C, Bianchi T, Zucchetti M. A survey of landmine detection using hyperspectral imaging. ISPRS Journal of Photogrammetry and Remote Sensing. 2017; 124: 40–53.
  72. Nikon 90D, Key Features. 2018. Available online at: <https://www.nikonusa.com/en/nikon-products/product-archive/dslr-cameras/d90.html>
  73. Sony α6000, Quicker autofocus than a DSLR. 2018. Available online at: [https://www.sony.com/electronics/interchangeable-lens-cameras/ilce-6000-body-kit#product\\_details\\_default](https://www.sony.com/electronics/interchangeable-lens-cameras/ilce-6000-body-kit#product_details_default)
  74. DuncanTech. MS2100, MS2150 & MS3100 Digital Multispectral Camera, User Manual. 2001. Available online at: [http://prom-sys.com/pdf/MS3100\\_manual.PDF](http://prom-sys.com/pdf/MS3100_manual.PDF)

75. DuncanTech. MS4000 and MS4100 High-Resolution Digital Color and Multispectral, User Manual. 2002. Available online at: [http://prom-sys.com/pdf/MS4000 & 4100 manual.PDF](http://prom-sys.com/pdf/MS4000_&_4100_manual.PDF)
76. Herman J, Evans R, Cede A, Abuhassan N, Petropavlovskikh I, et al. Comparison of ozone retrievals from the Pandora spectrometersystem and Dobson spectrophotometer in Boulder, Colorado. *Atmospheric Measurement Techniques*. 2015; 8: 3407-3418.
77. Czegan DAC, Hoover DK. UV–Visible Spectrometers: Versatile Instruments across the Chemistry Curriculum. *Journal of Chemical Education*. 2012; 89: 304-309.
78. PCO Imaging Pixelfly high performance digital 12bit CCD camera system. 2009. Available online at: [https://www.pco.de/fileadmin/user\\_upload/db/products/datasheet/pixelfly\\_20090505.pdf](https://www.pco.de/fileadmin/user_upload/db/products/datasheet/pixelfly_20090505.pdf)
79. Schlaepfer D. PARAmetric Geocoding, Orthorectification for Airborne Scanner Data, User Manual Version 2.3. ReSe Applications Schlaepfer and Remote Sensing Laboratories (RSL) of the University of Zurich. 2006.
80. Schläpfer D, Schaepman EM, Itten IK. PARGE: Parametric Geocoding Based on GCP-Calibrated Auxiliary Data. *Imaging Spectroscopy IV*. San Diego, US. 1998.
81. Luo J, Joshi D, Yu J, Gallagher A. Geotagging in multimedia and computer vision—a survey. *Multimedia Tools and Applications*. 2010; 51: 187–211.
82. Donato G, Belongie S. Approximate Thin Plate Spline Mappings. *Lecture Notes in Computer Science*. 2002; 21–31.
83. Han J, Kwon JH, Lee I, Choi K. Position and Attitude Determination for UAV-Based GPS, IMU and AT without GCPs. In *Proceedings of the International Workshop on Multi-Platform/Multi-Sensor Remote Sensing and Mapping*. Xiamen, China. 2011.
84. Micheletti N, Chandler JH, Lane, Stuart N. Section 2.2.2: Structure from Motion (SfM) Photogrammetry. In: Cook SJ, Clarke LE, Nield JM, editors. *Geomorphological Techniques (Online Edition)*. London: British Society for Geomorphology. 2015.

85. Wolf PR, Dewitt BA. Elements of Photogrammetry, with Applications in GIS, 3th edn. US: McGraw-Hill. 2000.
86. Höhle J. DEM Generation Using a Digital Large Format Frame Camera. Photogrammetric Engineering & Remote Sensing. 2009; 75: 87–93.
87. MITRE. Image Quality from the Natural Scene (IQM). Available online at: <http://www2.mitre.org/tech/mtf/>
88. FAS. National Image Interpretability Rating Scales (NIRS). 1998. Available online at: <https://fas.org/irp/imint/niirs.htm>
89. FAS. National Image Interpretability Rating Scales (NIRS). Civil NIIRS Reference Guide. 1998. Available online at: [https://fas.org/irp/imint/niirs\\_c/index.html](https://fas.org/irp/imint/niirs_c/index.html)
90. Johnson J. Analysis of image forming systems, in Image Intensifier Symposium, AD 220160 (Warfare Electrical Engineering Department, U.S. Army Research and Development Laboratories, Ft. Belvoir, Va., 1958; 244–273. Available online at: <https://www.cis.rit.edu/~cnspci/references/johnson1958.pdf>
91. Sjaardema TA, Smith CS, Birch GC. History and Evolution of the Johnson Criteria, SANDIA Report, Approved for public release, further dissemination unlimited, Sandia National Laboratories. Albuquerque, USA. 2015. Available online at: <https://prod-ng.sandia.gov/techlib-noauth/access-control.cgi/2015/156368.pdf>
92. Brook A, Dor EB. Supervised vicarious calibration (SVC) of hyperspectral remote-sensing data. Remote Sensing of Environment. 2011; 115: 1543-1555.
93. Secker J, Staenz K, Gauthier RP, Budkewitsch P. Vicarious calibration of airborne hyperspectra sensors in operational environments. Remote Sensing of Environment. 2001; 76: 81–92.
94. Spectral Imaging LTD. ImSpector imaging spectrograph user manual, version 2.21. 2003.
95. Miljković V, Gajski D. Adaptation of Industrial Hyperspectral Line Scanner for Archaeological Applications, The International Archives of the Photogrammetry. Remote Sensing and Spatial Information Sciences, Volume XLI-B5, 2016 XXIII ISPRS Congress. Prague, Czech Republic. 2016; 343-345.

96. Holst GC. CCD arrays, cameras and displays. Bellingham: SPIE Optical Engineering Press. 1998.
97. Kuittinen R. Transportable Test-Bar Targets and Microdensitometer Measurements-A Method to control the Quality of Aerial Imagery. International Archives of Photogrammetry and Remote Sensing. 1996; 31: 99–104.
98. ITT Enidine Inc., Wire Rope Isolator Technologies. 2019. Available online at: [http://www.itt-infrastructure.com/CorporateSite/media/itt/Resources/TechnicalData/WR\\_Catalog\\_2012.pdf?ext=.pdf](http://www.itt-infrastructure.com/CorporateSite/media/itt/Resources/TechnicalData/WR_Catalog_2012.pdf?ext=.pdf)
99. Lewis A. Current status of BAOAC (Bon Agreement Oil Appearance Code). Report to the Netherlands North Sea Agency. 2007.